

# Journal of Geophysical Research: Atmospheres

## RESEARCH ARTICLE

10.1002/2014JD021507

**Key Points:**

- Nabro volcano direct stratospheric injection is comparable to Sarychev Peak
- Volcanic stratospheric aerosol abundance is biased low in OSIRIS data set
- Sources of low bias in OSIRIS stratospheric aerosol are identified

**Supporting Information:**

- Readme
- Data Set S1
- Figure S1
- Figure S2
- Figure S3
- Figure S4
- Figure S5
- Figure S6
- Figure S7
- Figure S8

**Correspondence to:**

M. Fromm,  
mike.fromm@nrl.navy.mil

**Citation:**

Fromm, M., G. Kablick III, G. Nedoluha, E. Carboni, R. Grainger, J. Campbell, and J. Lewis (2014), Correcting the record of volcanic stratospheric aerosol impact: Nabro and Sarychev Peak, *J. Geophys. Res. Atmos.*, 119, 10,343–10,364, doi:10.1002/2014JD021507.

Received 17 JAN 2014

Accepted 30 JUL 2014

Accepted article online 4 AUG 2014

Published online 3 SEP 2014

## Correcting the record of volcanic stratospheric aerosol impact: Nabro and Sarychev Peak

**M. Fromm<sup>1</sup>, G. Kablick III<sup>1</sup>, G. Nedoluha<sup>1</sup>, E. Carboni<sup>2</sup>, R. Grainger<sup>2</sup>, J. Campbell<sup>3</sup>, and J. Lewis<sup>4</sup>**

<sup>1</sup>Remote Sensing Division, Naval Research Laboratory, Washington, District of Columbia, USA, <sup>2</sup>COMET, Atmospheric, Oceanic and Planetary Physics, University of Oxford, Oxford, UK, <sup>3</sup>Marine Meteorology Division, Naval Research Laboratory, Monterey, California, USA, <sup>4</sup>Joint Center for Earth Systems Technology, University of Maryland Baltimore County, Baltimore, Maryland, USA

**Abstract** Since 2010, several papers have been published that reveal a pattern of discrepancies between stratospheric aerosol data from the Optical Spectrograph and Infrared Imaging System (OSIRIS) instrument and other measurements and model simulations of volcanic plumes from Kasatochi, Sarychev Peak, and Nabro volcanoes. OSIRIS measurements show two discrepancies, a posteruption lag in aerosol onset/increase and a low bias in maximum stratospheric aerosol optical depth. Assumed robustness of the OSIRIS data drove various conclusions, some controversial, such as the contention that the June 2011 Nabro plume was strictly tropospheric, and entered the stratosphere indirectly via the Asian monsoon. Those conclusions were driven by OSIRIS data and a Smithsonian Institution report of strictly tropospheric injection heights. We address the issue of Nabro's eruption chronology and injection height, and the reasons for the OSIRIS aerosol discrepancies. We lay out the time line of Nabro injection height with geostationary image data, and stratospheric plume evolution after eruption onset using retrievals of sulfur dioxide and sulfate aerosol. The observations show that Nabro injected sulfur directly to or above the tropopause upon the initial eruption on 12/13 June and again on 16 June 2011. Next, OSIRIS data are examined for nonvolcanic and volcanically perturbed conditions. In nonvolcanic conditions OSIRIS profiles systematically terminate 1–4 km above the tropopause. Additionally, OSIRIS profiles terminate when 750 nm aerosol extinction exceeds  $\sim 0.0025 \text{ km}^{-1}$ , a level that is commonly exceeded after volcanic injections. Our findings largely resolve the discrepancies in published works involving OSIRIS aerosol data and offer a correction to the Nabro injection-height and eruption chronology.

### 1. Introduction

Bourassa *et al.* [2012] (hereafter B12) presented evidence, primarily based on the Optical Spectrograph and Infrared Imaging System (OSIRIS) aerosol data set, that appeared to show a delayed onset of stratospheric aerosol attributable to the eruption of Nabro volcano in northeast Africa ( $13.4^\circ\text{N}, 41.7^\circ\text{E}$ ) in June 2011. The roughly 18 day lag between the eruption onset and stratospheric OSIRIS aerosol [B12], combined with a partial isolation of the plume within the confines of the Asian monsoon anticyclone (within which Nabro is situated), weighed heavily on their provocative conclusion that the initial eruption's (12–13 June 2011) injection altitude was strictly tropospheric and that the introduction of volcanic particles to the stratosphere was solely by way of the Asian monsoon convection and dynamics. Two Technical Comments challenging B12 were published by Vernier *et al.* [2013] and Fromm *et al.* [2013] (hereafter V13 and F13, respectively). These rebuttals showed a variety of satellite data (not OSIRIS) characterizing the initial eruption day and stratospheric measurements in the first week after the eruption. The rebuttals, using the same stratospheric boundary benchmark as B12 (the 380 K potential temperature ( $\theta$ ) surface [Holton *et al.*, 1995]), revealed evidence of a stratospheric perturbation in volcanic sulfur dioxide ( $\text{SO}_2$ ) and particles apparently much sooner than OSIRIS did, as soon as 1 day after eruption onset. Curiously, in their accompanying Technical Comment Bourassa *et al.* [2013] identified "many stratospheric  $\text{SO}_2$  enhancements" in Microwave Limb Sounder data within a week of the Nabro eruption. None of the above-cited papers directly addressed three fundamental aspects of the link between Nabro emissions and the Asian monsoon: (1) the Nabro eruption chronology, (2) the quality of OSIRIS aerosol data, and (3) the survivability of tropospheric, aqueous  $\text{SO}_2$ , and hygroscopic sulfate particles in moist convection. Issues 1 and 2 are the aim of this study. Issue 3 is outside this study's scope.

Regarding the Nabro eruption sequence, the record is both incomplete and conflicting. Nabro eruption details in the Smithsonian Institution Global Volcanism Program's (SIGVP; <http://www.volcano.si.edu/>) activity report, which is often cited for such information, gives disparate start times for the eruption onset, from 00:00 UTC (source: Toulouse Volcano Ash Advisory Center) to 21:00 UTC 13 June (source: eyewitnesses) [SIGVP, 2011]. SIGVP gives an injection height on 13 June of 9.1–13.7 km (all heights above mean sea level; ASL), which is seemingly at odds with the much higher injection heights determined by V13 and the finding of Nabro aerosols on 14 June at 15–17 km over southern Israel [Sawamura *et al.*, 2012]. Tupper and Wunderman [2009] draw attention to the unsatisfactory status of injection-height information that is recorded by SIGVP and call for collaborative measures to improve these records. Neither B12, V13, F13 nor any other publications to our knowledge have given a full characterization of the Nabro eruption sequence and injection height. B12 only cited SIGVP; V13 and F13 presented only satellite-image snapshots of the eruption. In section 2 we establish the eruption sequence between 12 and 16 June using geostationary satellite data at 15 min resolution and plume altitude using nadir view SO<sub>2</sub> plume height retrievals and limb-profiling satellite data. These data together exhibit consistent evidence of immediate stratospheric penetration, a widespread stratospheric plume on 13 June, and a second stratospheric injection on 16 June.

Regarding OSIRIS aerosol data concerns, B12 stated that stratospheric Nabro aerosols began in abundance on 1 July. Yet three additional Nabro-related papers presented potential discrepancies with OSIRIS: much earlier observation of stratospheric aerosol or SO<sub>2</sub>. Sawamura *et al.* [2012] showed the aforementioned lidar measurement in southern Israel on 14 June. Uchino *et al.* [2012] reported two stratospheric aerosol layers over Japan on 20 and 23 June. Clarisse *et al.* [2014] presented daily maps of stratospheric SO<sub>2</sub> plume height starting on 13 June. V13, F13, and the three above-mentioned papers showed measurements of stratospheric particles and SO<sub>2</sub> at native Level 2 instrument resolution, whereas B12 employed spatiotemporal averages of OSIRIS aerosol extinction ratio or optical depth (AOD). Hence, the following questions are prompted. What would native-resolution OSIRIS data show in the first days after the Nabro eruption? Does the OSIRIS data set offer sufficient sampling, resolution, and sensitivity to accurately capture a young, concentrated particulate plume in the stratosphere? If the answer is affirmative, how can the apparent discrepancies between OSIRIS and the data employed by Sawamura *et al.* [2012], Uchino *et al.* [2012], Clarisse *et al.* [2014], V13 and F13 be reconciled? If not, what are the implications for the conclusions reached by B12 and other papers wherein OSIRIS aerosol data are used to characterize stratospheric volcanic impact?

Prior to the Nabro eruption of 2011, two volcanic eruptions relevant to the above questions occurred with direct stratospheric injection of gases and particles: Kasatochi (Aleutians) in August 2008 [Fee *et al.*, 2010] and Sarychev Peak (Kurile Islands) in June 2009 [Rybin *et al.*, 2011]. These eruptions were the subject of multiple papers involving OSIRIS aerosol data: Kasatochi by Bourassa *et al.* [2010] and Kravitz *et al.* [2010] (hereafter K10); Sarychev Peak by Haywood *et al.* [2010] (hereafter H10), Kravitz *et al.* [2011] (hereafter K11), O'Neill *et al.* [2012] (hereafter O12), and Jégoü *et al.* [2013]. The findings in K10, K11, H10, and O12 exposed discrepancies between OSIRIS stratospheric aerosol and comparative measurements or model output. In short, the discrepancies were twofold: a low bias in OSIRIS AOD and a delayed onset of peak AOD after the injection date. Each paper went to substantial length to resolve the discrepancies, but none arrived at a satisfactory explanation. It is noteworthy that Figure 4 of B12 shows a time rate of increase of Nabro OSIRIS stratospheric AOD that is greater than for the direct-injection scenarios of Kasatochi and Sarychev Peak. Was there in fact an unusual delay in the onset of Nabro stratospheric aerosols? Might there be a unifying explanation for the Nabro, Kasatochi, and Sarychev Peak discrepancies not reported in these papers?

In sections 2.5 and 3 we directly address the interplay between OSIRIS aerosol data and the evolution of stratospheric volcanic plumes. Our analysis primarily entails the use of OSIRIS version 5.07 data at its native profile sampling and resolution (downloaded from <http://osirus.usask.ca/>). The aim is to understand how completely the OSIRIS data set captures the transport pathway of sudden troposphere-to-stratosphere transport and plume evolution. Two volcanic events form the basis of our analysis, the Nabro and Sarychev Peak eruptions in mid-June 2011 and 2009, respectively. We will invoke independent aerosol data sets such as ground- and space-based aerosol lidar as a check on OSIRIS aerosol extinction profiles and AOD.

## 2. The Nabro Eruption Sequence—12 to 16 June 2011

### 2.1. Data

To characterize the Nabro eruption, we employ four satellite data sources and ground-based lidar. All but one have been used in prior publications on the Nabro eruption. Here we combine them to demonstrate two direct stratospheric injections imposed on a continuous, multiday eruption.

High temporal and spatial coverage of the 3 day interval is afforded by geostationary infrared imaging data from the Meteosat Second Generation (MSG) Spinning Enhanced Visible and Infrared Imager (SEVIRI)/Meteosat-9 11  $\mu\text{m}$  brightness temperature (BT), with 15 min temporal and 3 km spatial resolution. SEVIRI radiometric error at 10.9  $\mu\text{m}$  is 0.3 K at 300 K [Schmetz *et al.*, 2002]. These data were used to establish the overshooting nature and stratospheric penetration of the Nabro eruption on 12 June 2011 [V13].

Polar-orbiting hyperspectral infrared image data from the Infrared Atmospheric Sounding Interferometer (IASI) on board MetOp-A [Hilton *et al.*, 2012] sampled the Nabro environs twice daily. We introduce IASI SO<sub>2</sub> and SO<sub>2</sub>-altitude retrievals [Carboni *et al.*, 2012, and references therein] as an independent detector of Nabro's plume and injection height. MetOp-A is in a Sun-synchronous orbit with local overpass time at approximately 09:30 and 21:30, delivering twice-daily mapping opportunities at a given location. IASI retrievals of SO<sub>2</sub> attributable to volcanoes and anthropogenic pollution were the subject of Karagulian *et al.* [2010] and Clarisse *et al.* [2011], respectively. Carboni *et al.* [2012] took the additional step of retrieving height of a SO<sub>2</sub> plume and testing the retrieval on the eruption plume from Eyjafjallajökull volcano in April/May 2010.

The IASI retrieval is an optimal estimation approach applied to SO<sub>2</sub> absorption bands at 7.3 and 8.7  $\mu\text{m}$ . Carboni *et al.* [2012] found that the uncertainty in the SO<sub>2</sub> amount and height retrieval was inversely proportional to SO<sub>2</sub> abundance and plume altitude. For example, for a plume with > 2 Dobson unit (DU) SO<sub>2</sub> at altitudes > 8 km, SO<sub>2</sub> concentration and height uncertainty are less than 1 DU and 1 km, respectively. When the measurements do not contain enough information to retrieve all the parameters (e.g., a small SO<sub>2</sub> amount), the retrieved values converge toward the a priori value, as will the corresponding error. In this work we are using the same a priori values as Carboni *et al.* [2012], in particular 0.5 DU and 400 mb as a priori amount and altitude, respectively, and 100 DU and 500 mb as a priori uncertainty, respectively. Where there is not enough information to retrieve the altitude, the resulting value is the a priori. In the upcoming analyses, these occurrences are evident at the periphery of a high-altitude plume. Our application of IASI SO<sub>2</sub> plume height data to a suspected stratospheric injection is new, and the results in isolation might thus be in doubt. But once validated against the other instruments, they provide distinct advantages in terms of horizontal and temporal coverage. We will present the Level 2 IASI retrievals with no screening, except for the condition that SO<sub>2</sub> > 0 DU and SO<sub>2</sub> height > 5 km.

Satellite-based vertical profiles of SO<sub>2</sub> and aerosols are provided by NASA's Aura Microwave Limb Sounder (MLS) [Waters *et al.*, 2006] and Cloud Aerosol Lidar with Orthogonal Polarization (CALIOP) [Winker *et al.*, 2009], respectively. MLS and CALIOP, in NASA's A-Train formation, make their measurements less than 10 min apart (<http://atrain.nasa.gov/>). MLS SO<sub>2</sub> is retrieved between 215 and 10 hPa [Livesey *et al.*, 2011]. The MLS vertical/horizontal resolution is 3/170 km, respectively. CALIOP vertical/horizontal resolution is 0.06/1.0 km at altitudes between 8.2 and 20.2 km. The Version 3.3 MLS SO<sub>2</sub> product is available. However, presently, no validation of the data has been published (W. Read, personal communication, 2013). F13 showed stratospheric MLS SO<sub>2</sub> enhancements on the day and week after Nabro's eruption onset that were spatially and temporally consistent with the V13 CALIOP results.

A ground-based Micro Pulse Lidar Network instrument (532 nm) [Welton *et al.*, 2001] at Sde Boker, Israel (30.85°N, 34.78°E), operated continuously before and during the Nabro eruption. Sde Boker is strategically located such that the stratospheric and tropospheric particulate volcanic emissions were captured within 1 day of the eruption onset [Sawamura *et al.*, 2012]. We use the native backscatter data at 0.075 km vertical and 1 min temporal resolution.

### 2.2. Tropopause Height

In this section and throughout this paper, we will adopt two methods for tropopause height determination. When dealing with tropical latitudes, the tropopause is taken to be 17 km [Gettelman *et al.*, 2011]. For extratropical latitudes, we use the dynamical definition, i.e., based on potential vorticity (pv). Unless otherwise specified, we use the pv = 3 pvu threshold for tropopause height. Calculations are made using

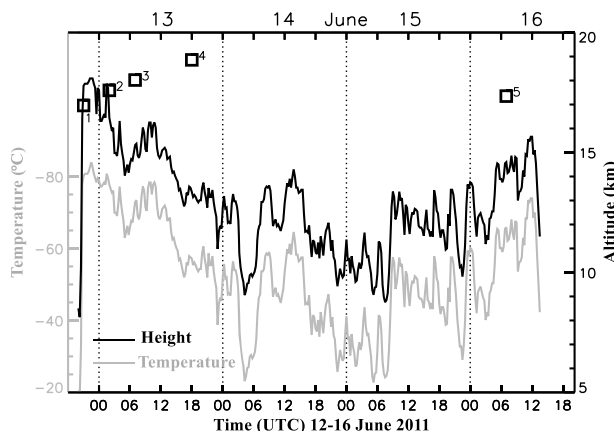


**Figure 1.** Time series of SEVIRI 11  $\mu\text{m}$  brightness temperature minimum and cloud top height in a  $30 \times 45$  km box surrounding Nabro volcano, from 18:00 UTC 12 June to 18:00 UTC 16 June 2011. Temporal resolution of the SEVIRI data is 15 min. Temperature on the left ordinate is reversed for consistency with cloud top altitude. Vertical bars separate UT days. The numbered black squares represent the altitude at Nabro coincidence time of the five aerosol or  $\text{SO}_2$  observations listed in Table 1 and discussed in the text.

that BT-inferred volcanic cloud heights were stratospheric: between 15 and 17 km. This is indeed a low estimate considering that Bourassa *et al.* [2010]—who state that “the Kasatochi eruption injected approximately 2.0 Tg of  $\text{SO}_2$  into the lower stratosphere”—reported volcanic aerosols as high as 15–21 km thereafter.

Figure 1 is a time series of  $\text{BT}_{\min}$  and inferred cloud top height, in a  $30 \times 45$  km box surrounding Nabro volcano from 18:00 UTC on 12 June to 18:00 UTC on 16 June 2011. Cloud top height was inferred from  $\text{BT}_{\min}$  via linear interpolation using radiosonde temperature/height data from Abha, Saudi Arabia ( $18.23^\circ\text{N}, 42.65^\circ\text{E}$ ). An animation of the BT map for this period is contained in the supporting information. Although we are cognizant of the potential uncertainties in the TIR/injection-height association as described by Oppenheimer [1998, and references therein], this application of  $\text{BT}_{\min}$  primarily focuses on relative changes in eruption explosivity/height over time. The drop in temperature (and increase in cloud top height) shown in Figure 1 identifies the explosive, deep nature of the initial eruption on 12 June. Cloud temperature at 22:30 UTC 12 June is  $-84^\circ\text{C}$ , which is not significantly different than the Abha cold point ( $-82.3^\circ\text{C}$ , at 18.1 km)—the cold point being the absolute top of the tropical tropopause layer [Gettelman *et al.*, 2011]. At this early point in the Nabro eruption, MODIS and SEVIRI TIR data also exhibited a localized warm core in the cold cloud top, which V13 and F13 displayed and attributed to overshooting of the plume into the lowermost stratosphere. This situation (anomalously cold pixels and warm core area) involves greater uncertainty in the TIR/height determination, but it suggests that cloud tops are above tropopause level. From this point to the end of the time series,  $\text{BT}_{\min}$  is warmer than the cold point, obviating this complication. We will assume that the cloud top inferred by the  $\text{BT}_{\min}$  is located below the cold point, using only this part of the environmental profile for the temperature/height lookup. Cloud top temperature remains very low for several hours of 13 June, indicative of a continuous eruption to or near the tropopause. This is consistent with the tropopause-level cloud top pressure exhibited by the MODIS data shown in F13 and in the supporting information. Equally low cloud top pressure is seen from near the volcano (fresh injection) to distant points (hours-old emissions).

BT then increases between 14 and 16 June but remains lower than  $-20^\circ\text{C}$  and above 8 km altitude throughout. Although the 4 day interval does include some passages of meteorological cloud, the animation provided in the supporting information confirms that the vast majority of the BT signal is generated by volcanic emission. A second local BT minimum is recorded  $\sim 12:00$  UTC 16 June.  $\text{BT}_{\min}$  at that time was  $-74^\circ\text{C}$  ( $\sim 120$  hPa, 15.6 km).

In summary, the  $\text{BT}_{\min}$  time series shows a continuous volcanic convective cloud between 13 and 16 June, with injection heights ranging from 8 to 18 km, and an indication that there was a second deep injection

National Center for Environmental Prediction Reanalysis data [Kalnay *et al.*, 1996]. We also invoke the 380 K potential temperature level in some places, to be in conformity with cited works that used this stratospheric “overworld” definition [Holton *et al.*, 1995].

### 2.3. Geostationary Infrared

V13 used MSG IR data to establish that Nabro’s eruption had begun by 21:00 UTC 12 June 2011. We use MSG 11  $\mu\text{m}$  image data to construct a multiday time line of minimum brightness temperature ( $\text{BT}_{\min}$ ) from eruption onset through 16 June. The thermal IR (TIR) approach to cloud top estimation is considered to be biased low for tropical convective clouds, according to Hamada and Nishi [2010] and Sherwood *et al.* [2004]. Moderate resolution Imaging Spectrometer (MODIS) TIR was used to characterize the explosive eruption of Kasatochi by Fee *et al.* [2010]. They found

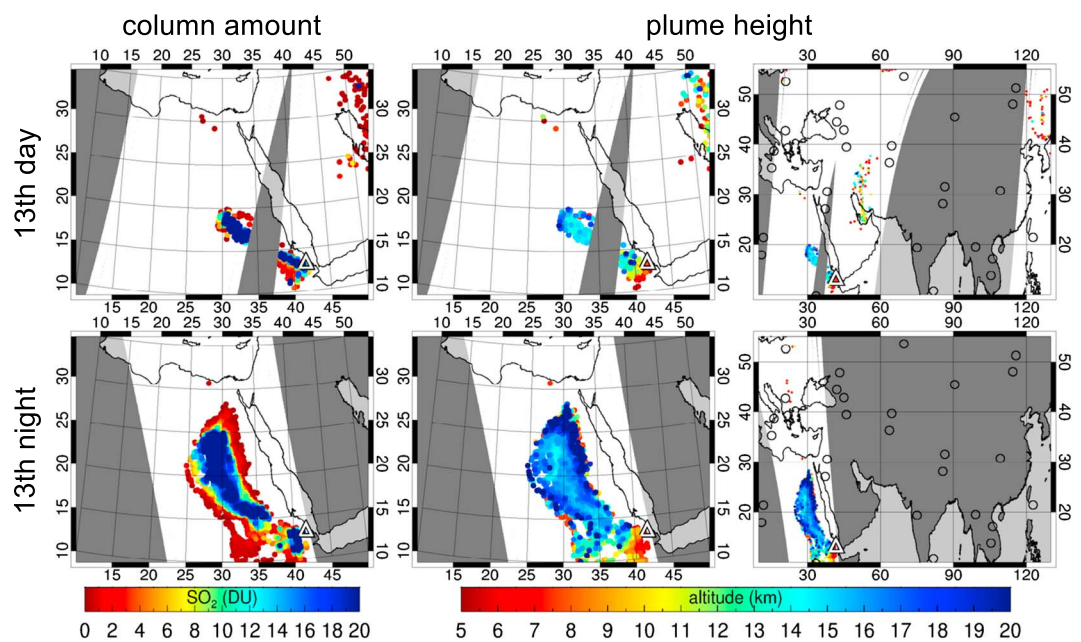


**Figure 2.** IASI SO<sub>2</sub> concentration (DU) and SO<sub>2</sub> height (km), 13 June 2011. (left and middle) SO<sub>2</sub> concentration and height, zoomed in on northeast Africa and the Middle East. Nabro location: white triangle. (right) SO<sub>2</sub> height in a domain including all of Asia. Maps in Figure 2 (right) show OSIRIS measurement locations (black circles) on each calendar day. White regions on the maps are IASI field-of-view locations without a retrieval. Gray-shaded regions signify interorbit or orbital data gaps.

from Nabro on 16 June. An independent view of the high plumes on 13 and 16 June, afforded by CO<sub>2</sub> slicing applied to Terra and Aqua MODIS data similar to Figure 1 in F13, is provided in the supporting information. Next we will present evidence that the 13 and 16 June eruption pulses impacted the lowermost stratosphere and that the plume top is underestimated by the BT-inference approach. In section 2.4 we will discuss the five black boxes in Figure 1.

#### 2.4. IASI, CALIOP, MLS, and MPLNET

An independent view of plume injection altitude is afforded by IASI SO<sub>2</sub> height retrievals. Our analysis combines IASI with three independent and coincident measurements of SO<sub>2</sub> abundance, height, and volcanic aerosols to assess the robustness of the IASI plume height information. The IASI SO<sub>2</sub> concentration and height retrievals between 13 and 18 June are mapped in Figures 2–7. The initial Nabro plume shows up strongly during daytime 13 June. The two separate plume features are the result of an interorbit data gap. SO<sub>2</sub> concentration in the plume, which is entirely over northeast Africa on both daytime and nighttime IASI overpasses, is greater than 20 DU over an expansive area where the plume altitude is between ~14 and 18 km.

On 14 June (Figure 3) the plume spread into the Middle East and much of the plume has top altitudes above ~14 km. On 15 June (Figure 4) the plume stretched from near the volcano to Central Asia, under the influence of the continuous eruption discussed in section 2.3. The plume is exhibiting a separation of equally long higher- and lower altitude segments north and south, respectively. On 15 and 16 June (Figure 5) the plume remains anchored to the volcano and arcs north and east as far as Mongolia and China. The western edge of the high-altitude segment (now clearly separated from the lower material) remains over northern Africa. Indeed B12, using CALIOP backscatter data, identified in their Figure S2 this segment of the long plume as a “small stratospheric layer” at 19 km, and F13 traced it via trajectory to Nabro’s 13 June eruption. The line of this CALIOP overpass is shown on the maps of Figure 4 (bottom row). On 17 June (Figure 6) the southern, lower altitude stream of material is now punctuated by a high-altitude feature stretching from northeast Africa into the Middle East. High-altitude retrievals are still evident in the northern stream of material, enveloped in a plume that is continuous from the Mediterranean Sea to East Asia.

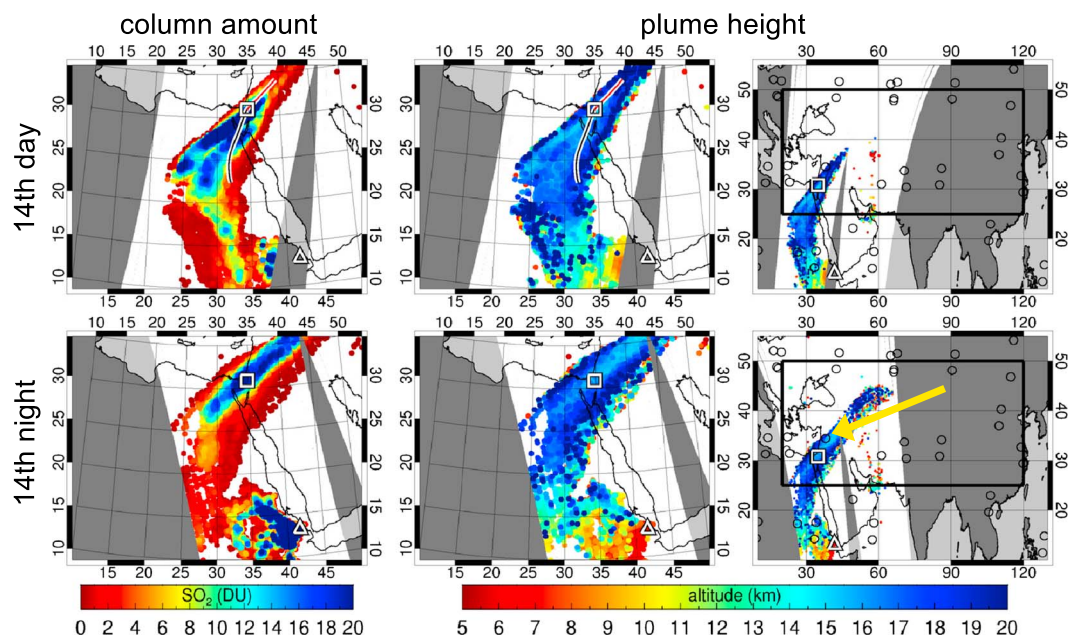


**Figure 3.** As in Figure 2 but for 14 June 2011. Sde Boker's location is indicated by a white square. The red and black lines are the respective Hybrid Single-Particle Lagrangian Integrated Trajectory (HYSPLIT) forward and backward trajectories initialized at Sde Boker discussed in section 2.4. The large box in the right column maps is the area inside which OSIRIS profiles are selected for Figure 10. Yellow arrow points to an OSIRIS profile within the plume discussed in Figure 10.

We verify the IASI plume-height data by comparing with height-resolved, independent, near-coincident aerosol and SO<sub>2</sub> data. For the first stratospheric injection, we show in Figure 8 the IASI morning and night 14 June measurements of the plume and aerosol data from the Sde Boker lidar, which is part of the Micro Pulse Lidar Network (MPLNET). Stratospheric aerosols from Nabro were detected continuously at Sde Boker [Sawamura et al., 2012] for approximately 24 h from approximately 03:00 UTC 14–15 June. Tropopause height based on  $p_v = 2$  and 3  $p_{vu}$  is shown to convey uncertainty. The tropopause is between 15 and

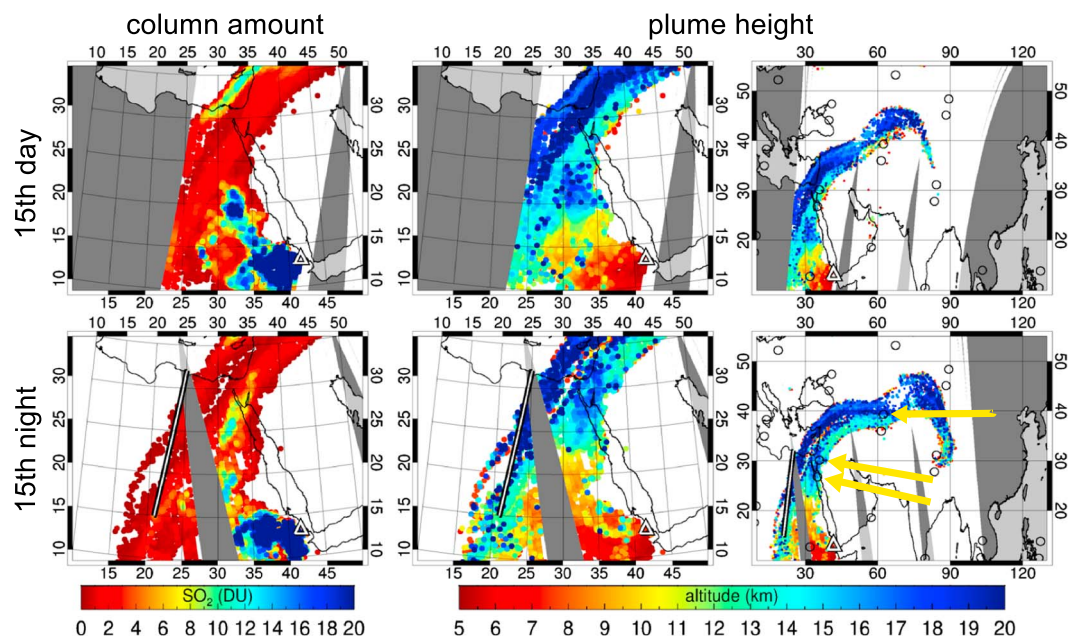


**Figure 4.** As in Figure 2 but for 15 June 2011. The CALIOP orbit segment discussed in section 2.4 is shown in the bottom three panels. Yellow arrows point to OSIRIS profiles discussed in Figure 10.

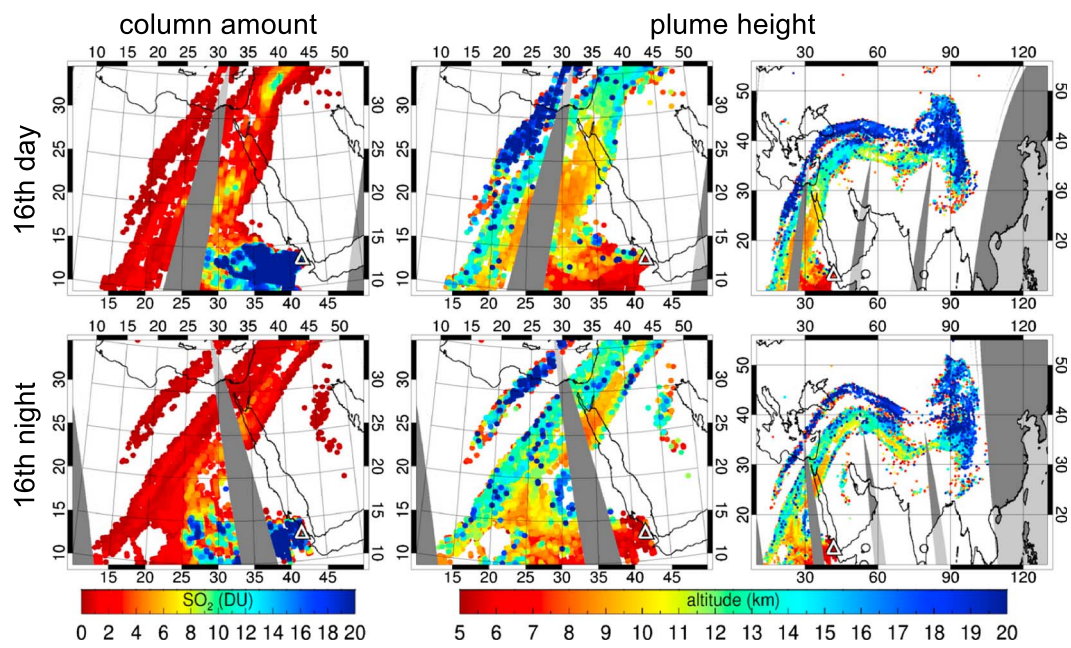


**Figure 5.** As in Figure 2 but for 16 June 2011.

16 km, 1–3 km lower than the highest aerosols. A layer near the tropopause is evident between ~12:00 UTC 14 June and 00:00 UTC 15 June. Optically thinner layers are seen below the tropopause. At 07:40 and 18:56 UTC, IASI retrieved SO<sub>2</sub> and plume height near Sde Boker (Figure 3). The SO<sub>2</sub> plume heights for coincident (within 0.5° latitude and longitude) IASI pixels at 07:40 UTC span the aerosol layer within ~1 km, with a clumping near the bottom of the scattering layer. At 18:56 UTC the IASI heights are roughly the same as the morning data and span the lower of two Nabro layers, near the tropopause.

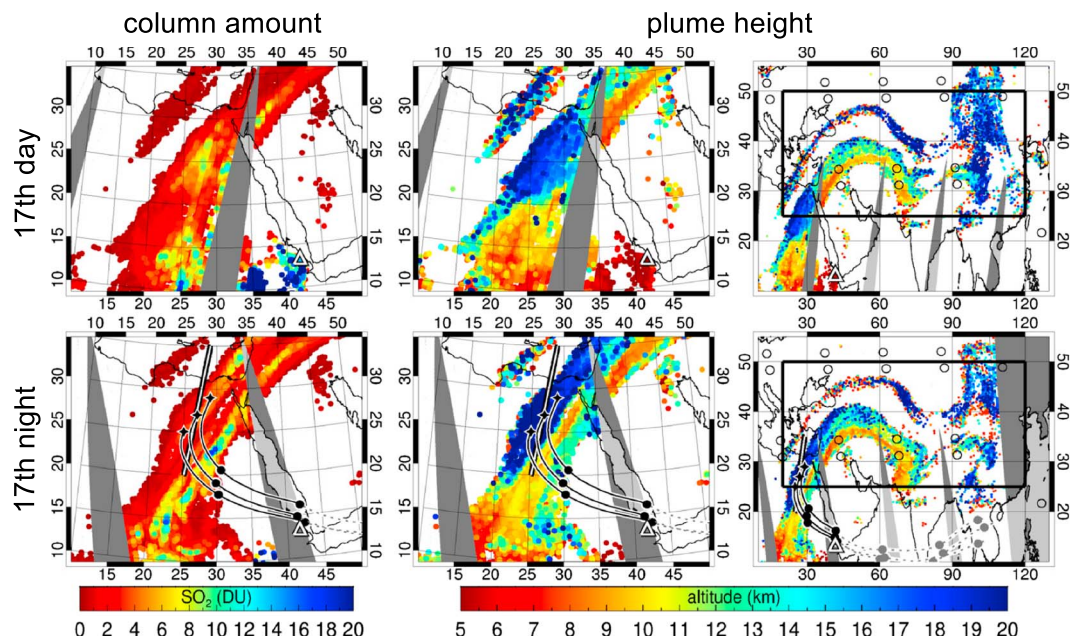


**Figure 6.** As in Figure 2 but for 17 June 2011. Box in right column maps same as in Figure 3. Nighttime maps have a line showing CALIOP/A-Train overpass at ~00:00 UTC 18 June and have 5 day isentropic back trajectories launched in the IASI SO<sub>2</sub> plume straddling the A-Train swath. Trajectories are initialized at 19:00 UTC 17 June at 17 km ASL (~389 K potential temperature) at 25°N, 25°E; 27°N, 27°E; and 29°N, 29°E. Dotted trajectory segments, pre-16 June; solid segments, post 00:00 UTC 16 June. Black dots give 00:00 UTC positions.

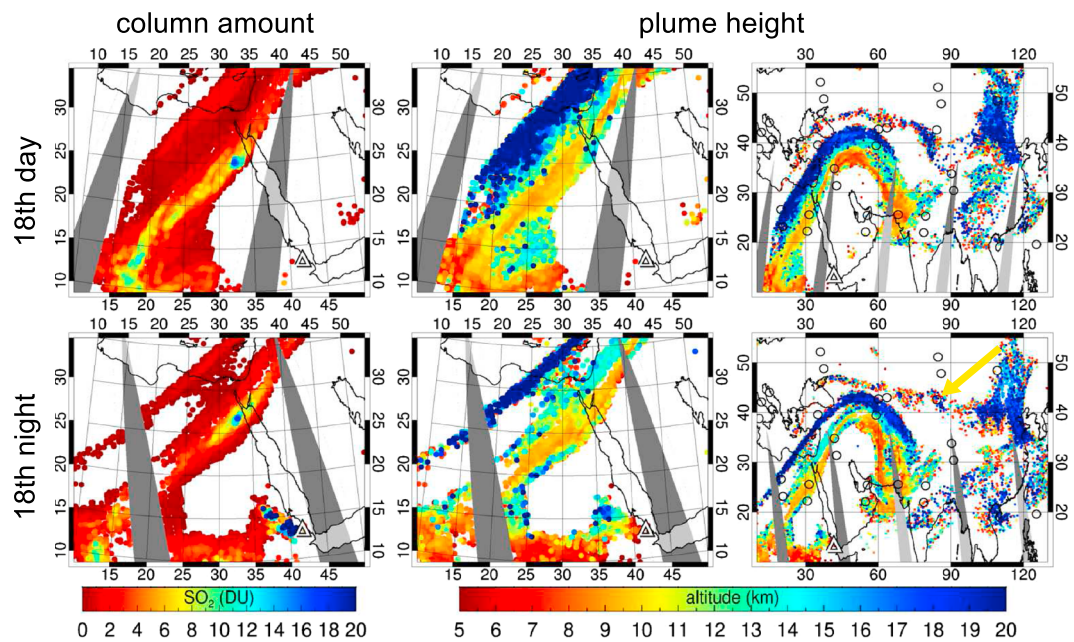


**Figure 7.** As in Figure 2 but for 18 June 2011. Yellow arrow points to OSIRIS profile within the plume discussed in Figure 10.

Figure 3 shows forward and backward isentropic trajectories initialized at Sde Boker at 03:00 UTC on 14 and 15 June used for the initial and terminal detection of stratospheric aerosol, respectively. Trajectory calculations here and throughout are from the Hybrid Single-Particle Lagrangian Integrated Trajectory (HYSPLIT) model [Draxler and Rolph, 2013]. The forward trajectory, northeast of Sde Boker, shows that the stratospheric aerosols initially detected conform with the leading edge (i.e., the northeastward extent) of the IASI  $\text{SO}_2$  plume feature. The backward trajectory (southwest of Sde Boker) shows that the termination of stratospheric aerosol detection conforms with another perimeter location of the IASI plume. Taken together, the lidar, IASI, and wind data give a coherent picture of stratospheric  $\text{SO}_2$  and particulates consistent with a direct, multihour stratospheric injection on 12/13 June, as illustrated in Figure 1. The lidar data also give a compelling verification of the IASI  $\text{SO}_2$  height retrievals for a subtropical upper troposphere/lower stratosphere (UTLS) volcanic plume.

The stratospheric Nabro plume generated by the eruptive pulse on 16 June is the focus of our second IASI comparison. The nighttime 17 June IASI overpass (Figure 6, bottom row) of northeastern Africa was at

19:30 UTC, approximately 5 h prior to the overpass of the A-Train. At this time/location, the Nabro  $\text{SO}_2$  plume is oriented toward the northeast similar to the prior days, with a high-altitude portion to the north and lower altitude  $\text{SO}_2$  to the south. A transect on Figure 6 (bottom row) shows the A-Train path over the Nabro plume between 20° and 35°N. Along this transect, IASI continuously detects  $\text{SO}_2$  up to ~6 DU as far north as ~30°N. The transect intersects both the low- and high-altitude part of the plume.

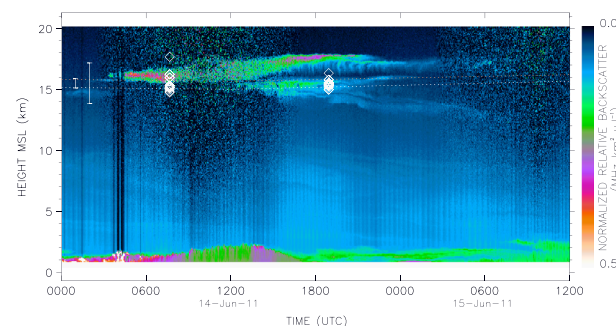


**Figure 8.** Time-height curtain of Sde Boker normalized relative backscatter, 00:00 UTC 14 June–12:00 UTC 15 June 2011. Lower (higher) dotted line is tropopause altitude based on the  $\text{pv} = 2$  (3)  $\text{pvu}$  threshold, respectively. White diamonds are IASI  $\text{SO}_2$  height retrievals within 0.5° latitude and longitude from Sde Boker. Error bars offset to left represent the average and maximum IASI uncertainty among the illustrated pixels. See text for details.

Figure 9 shows Level 2 MLS  $\text{SO}_2$  mixing ratio and CALIOP 532 nm attenuated backscatter through this portion of the Nabro plume. Figure 9 also contains the 380 K isentrope interpolated from

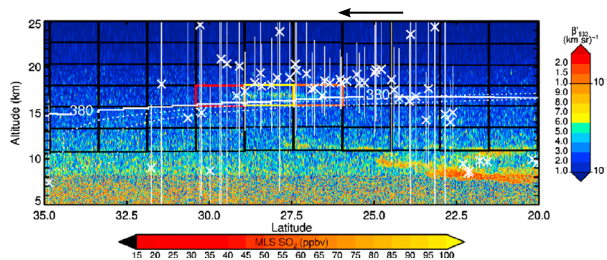


**Figure 9.** Latitude-height curtain along A-Train orbit ~00:00 UTC 18 June 2011 over northeast Africa. CALIOP 532 nm attenuated backscatter (color scale on right). Open rectangles represent MLS retrieval volumes colored according to  $\text{SO}_2$  mixing ratio (color scale along bottom). White line: 380 K isentrope. Lower (higher) dotted line is tropopause altitude based on the  $\text{pv} = 2$  (3) ppu threshold, respectively. IASI  $\text{SO}_2$  height: white cross. Arrow length is commensurate with  $1.86^\circ$  latitude movement in 5 h between A-Train and IASI using HYSPLIT trajectories that are also used for the 120 h path discussed in the text.

CALIOP measurements include 532 nm linear volume depolarization ratio, which is an indicator of particle shape (and by inference, liquid sulfate droplets). V13 discuss this, arguing that the Nabro sulfate droplets give near-zero depolarization. The particles detected in both the northern stratospheric and southern tropospheric segments of the CALIOP curtain in Figure 9 are nondepolarizing (not shown) and are therefore very likely liquid sulfate aerosols.

IASI  $\text{SO}_2$  and  $\text{SO}_2$  height retrievals accurately resolve both portions of the Nabro emissions. IASI  $\text{SO}_2$  heights are between the CALIOP tropospheric scattering layers toward the south, then increase northward, and are generally distributed  $\sim 1\text{--}2$  km above the MLS  $\text{SO}_2$  and CALIOP aerosols where the stratospheric anomaly is greatest. Wind direction at UTLS altitudes at this time were toward the north-northeast. Thus, the advection of volcanic material in the 5 h interval between IASI and MLS/CALIOP would be roughly along the line of the A-Train orbit, aiding in the reconciliation of the  $\text{SO}_2$  and aerosol-height gradients observed here. The arrow length in Figure 9 represents the distance an air parcel would traverse in the 5 h measurement interval.

Backward trajectories from the stratospheric portion of the IASI/MLS/CALIOP Nabro plume, terminating on 13 June, are shown in Figure 6 (bottom row). Trajectory paths are plotted as solid lines through 00 UTC 16 June and dotted back to 00 UTC 13 June. The paths go over Nabro. However, the Nabro overpass is on 16 June and clearly not 13 June—these endpoints are over distant southeastern Asia. Hence, this near-coincident combination of A-Train and IASI data reinforces the finding from Figures 1–7 that there was a second, distinct, injection to the tropopause region from Nabro volcano on 16 June. The totality of stratospheric Nabro emissions was attributable to two impulses, 3 days apart.

In the prior analysis, we presented back-trajectory evidence for direct stratospheric injection of particles and  $\text{SO}_2$ , showing advection paths to the volcano. We use the time of the Nabro overpass to annotate Figure 1, illustrating the altitude of the material transported isentropically from these downstream observations. Table 1 summarizes five distinct observation/trajecotry connections to Nabro. The Nabro-overpass symbols of these five height-resolved layers in Figure 1 are seen in the context of the TIR-determined volcanic cloud's optically opaque top altitude. The fact that isentropic transport produces a match for these five distinct observations with the volcano indicates an injection source term consistent with these overpass altitudes. In the case of the two Sde Boker observations 9 h apart on 14 June, the altitude is closely matched with the inferred heights of the TIR method. The other two matches on 13 June, and the match on 16 June, are at altitudes considerably greater than the BT-inferred cloud tops. Yet the  $\text{BT}_{\min}$  time series clearly shows two relatively deep injection scenarios, on 12–13 and 16 June. We conclude from this that the  $\text{BT}_{\min}$  approach here at brief intervals approximates the actual injection height but more generally underestimates the true stratospheric injection altitude.

In summary, the evidence shows that stratospheric gases and sulfate particles were in abundance on each day starting on 13 June and that there is close correspondence between the particulate and gaseous emissions. Hence, the synoptic view of the stratospheric plume evidenced by IASI  $\text{SO}_2$  and  $\text{SO}_2$  height retrievals

ERA-Interim reanalysis [Dee et al., 2011], tropopause height determined from  $\text{pv} = 2$  and 3 ppu, and IASI  $\text{SO}_2$  height retrievals that are within  $0.25^\circ$  of the CALIOP profile coordinates. MLS  $\text{SO}_2$  shows strong enhancement between  $\sim 26^\circ$  and  $30^\circ\text{N}$ , 16–18 km. The maximum  $\text{SO}_2$  mixing ratio here is  $>100$  ppbv while the pre-Nabro stratospheric MLS  $\text{SO}_2$  is  $\sim 0$  ppbv with a standard deviation of approximately 4 ppbv in the UTLS. Inside the relatively broad MLS pixels, CALIOP backscatter is enhanced above the 380 K level. Toward the south, and below the minimum MLS retrieval altitude, CALIOP backscatter is enhanced between  $\sim 7$  and 11 km.

**Table 1.** Nabro Stratospheric Layers Observed Between 14 and 18 June 2011

Figure 1 Number	Observation	Source	Measurement Altitude/ Potential Temperature (km ASL/K)	Nabro Overpass Altitude (km ASL)	Nabro Overpass Time
1	Sde Boker, 09 UTC 14 June	Figure 8	16.2/385	16.8	22 UTC 12 June
2	Sde Boker, 18 UTC 14 June	Figure 8	17.3/402	17.6	02 UTC 13 June
3	MLS 80 hPa SO <sub>2</sub> , 11 UTC 14 June	F13	18.0/411	18.0	07 UTC 13 June
4	CALIOP "small...layer," 00 UTC 16 June	F13; B12	18.7/435	18.9	18 UTC 13 June
5	CALIOP/MLS 00 UTC 18 June	Figure 9	17.0/393	17.4	07 UTC 16 June

can be used to follow the spreading aerosol plume in the days following the eruption and to assess the OSIRIS profile sampling of the young Nabro stratospheric plume.

## 2.5. OSIRIS, 13–18 June

V13 and F13, using vertical profiling instruments, showed the evolution of stratospheric aerosols and SO<sub>2</sub> in the week following Nabro's eruption onset. IASI data, in the right columns of Figures 2–7, give a synoptic view of the gaseous stratospheric and tropospheric Nabro emissions as they spread over the Middle East, Central, and Eastern Asia during and after the two deep impulses discussed in sections 2.3 and 2.4. These also show OSIRIS's native measurement coverage between 13 and 18 June. The number of OSIRIS profiles in the zone from the eastern Mediterranean to East Asia (defined as 25–50°N, 20–120°E) ranges between 0 and 18 per day. The nadir-imaging coverage of IASI permits an examination of the location of individual OSIRIS profiles with respect to the evolving plume (as was done for the Sde Boker MPLNET instrument in section 2.4).

Figure 10a displays the 17 OSIRIS aerosol extinction profiles in this zone on 14 June, compared with a 12 day sample of profiles collected prior to the Nabro eruption (1–12 June) and extinction values estimated at 750 nm from Sde Boker MPLNET data on the fourteenth. All but one OSIRIS profile in the 1–12 June sample

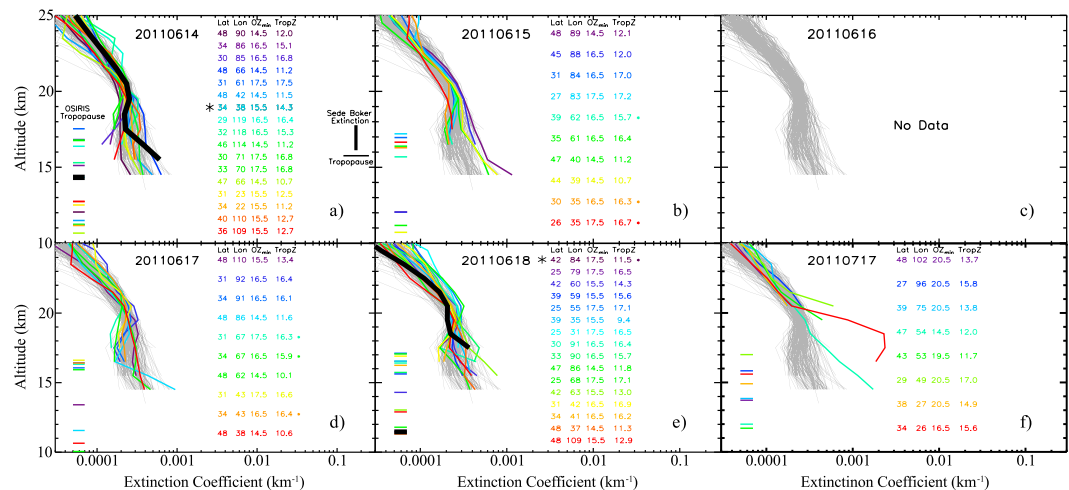


**Figure 10.** OSIRIS 750 nm aerosol extinction coefficient for pre- and post-Nabro time frames in a box bounded by 25°N–50°N, 20°E–120°E (see boxes in Figures 3 and 6). Pre-Nabro (gray profiles) is defined as 1–12 June 2011. Post-Nabro profiles are color coded to distinguish from pre-Nabro and one another. Listing gives the coordinates of each profile, its terminal altitude and tropopause height. Small horizontal bars show the collocated tropopause heights. Vertical bar on right is the maximum 750 nm extinction coefficient measured at Sde Boker at 16:00 UTC 14 June 2011, spanning the ~ 1.6 km thick aerosol layer between 16.1 and 17.8 km (see Figure 7). Horizontal bar below is the collocated tropopause height. (a) 14 June. (b) 15 June. (c) 16 June. (d) 17 June. (e) 18 June. (f) 17 July. Thick black lines and asterisks identify profiles discussed in detail in the text and highlighted in Figures 3 and 7. Colored asterisks indicate the profiles within the perimeter of the IASI SO<sub>2</sub> plume.

terminate at 14.5 km or higher, regardless of the local tropopause condition (average/minimum tropopause height = 12.7/9.3 km, respectively). The post-Nabro profiles in Figure 10 contain information on the profile termination height and the local tropopause. The exhibited pattern is fairly typical in background conditions (as will be quantified in section 3); OSIRIS profiles seldom probe below the tropopause and regularly terminate 0–4 km above a high tropopause, and more so when the tropopause is below ~10 km. It is evident that none of these profiles exhibit stratospheric aerosol extinction enhancement with respect to pre-Nabro. Looking at Figure 3, we see that this is attributable to sampling sparseness with respect to the day-old plume; one profile is located near the core of the high-altitude portion of the plume. This profile is targeted in Figure 10a, in bold black. The OSIRIS profile appears to be located within the stratospheric part of the Nabro plume. It terminates at 15.5 km, 1.2 km above the local tropopause. The average IASI plume height for pixels within 0.5° latitude and longitude is 16.4 km. Assuming that the OSIRIS measurement time is ~16:00 UTC (18 local standard time (LST)), the simultaneous layer at Sde Boker (~330 km south) is between ~16 and 18 km. We convert Sde Boker's backscatter to 750 nm extinction coefficient using the method of *Campbell et al.* [2008] and show the layer's maximum as a vertical bar on Figure 10a. Nabro's plume exhibits an extinction coefficient almost 3 orders of magnitude greater than the OSIRIS measurement.

If indeed the Sde Boker lidar data capture the height and optical properties of the synoptic IASI feature, it would be reasonable to expect that OSIRIS would resolve a similar extinction enhancement vis-à-vis background conditions. The fact that the OSIRIS profile terminates below the IASI and Sde Boker layers and gives no hint of such an enhancement suggests three possible explanations: (1) the Nabro aerosols at the time/location of the OSIRIS measurement were below the level at which the retrieval terminated, (2) the stratospheric part of the Nabro plume had not yet advected into the OSIRIS field of view, and (3) the lidar's 523 nm channel is more sensitive to the optical properties of the Nabro particle-size distribution than OSIRIS's 750 nm wavelength. Each explanation contributes to the point that spatiotemporal sampling and instrument sensitivity are critical to the correct characterization of a young/concentrated particulate phenomenon. In this case, Sde Boker's fortuitous observations reveal a critical aspect of the initial stratospheric Nabro injection that no satellite remote sensing measurement was able to capture.

Figure 10b shows OSIRIS profiles on 15 June. As for 14 June, there are no profiles exhibiting an apparent aerosol enhancement with respect to pre-Nabro, in spite of the fact that three of the profiles are located within the IASI SO<sub>2</sub> plume. They are identified with arrows in Figure 4 and asterisks in Figure 10b. The tropopause is high—greater than 15.7 km—near these profiles, as are the IASI plume-heights. The OSIRIS profiles terminate within 1 km above the tropopause. Hence, it is difficult to make firm conclusions, except that no obvious aerosol enhancement was evident in the OSIRIS profile. There were no OSIRIS measurements in this zone on 16 June (Figures 5 and 10c). Figure 10d shows the OSIRIS aerosol profiles in the same zone on 17 June, after the Nabro plume had spread into East Asia. There are no OSIRIS locations within the stratospheric plume suggested by the IASI map (Figure 6). There are three within the southern, lower stream (marked by asterisks in Figure 10d). The profiles terminate 0–4 km above the tropopause like they did on 14 and 15 June, and there are no extinction enhancements compared with preeruption background.

On 18 June (Figure 10e), an anomalous condition is evident in one of the OSIRIS profiles (42°N, 84°E). Here the profile exhibits no extinction enhancement but terminates higher than normal on an absolute scale (17.5 km) and tropopause-relative scale as well (6 km). It is located amidst a weakening IASI SO<sub>2</sub> feature (Figures 7) that had on the prior day comprised heights of ~16–18 km. CALIOP backscatter curtains [see *Clarisse et al.*, 2014] on this day bracketing the OSIRIS profile exhibit scattering layers ~16–18 km. It is shown next that high OSIRIS-profile termination increases in frequency in the immediate post-Nabro period.

Figure 10f shows the situation in the same geographic zone, 1 month after the eruption (17 July), at which time Nabro stratospheric aerosols abounded in Asia and had spread zonally around the globe [Sawamura *et al.*, 2012, B12]. There are eight profiles in this zone, all of which look different in two respects compared to the preeruption profiles (gray) and the posteruption profiles of Figures 10a–10e. One difference is that there are no posteruption profile measurements below 17.5 km within the gray preeruption envelope. Four profiles terminate more than 5 km above the tropopause; one above 20 km. Extinction in these apparently truncated profiles fall mostly into the preeruption envelope, although a few hint at an extinction enhancement near the profile termination altitude. The other difference is manifested by the one profile exhibiting a layer feature at 17.5–18.5 km with an approximate order-of-magnitude aerosol extinction increase. Hence, at this point in the plume's evolution, OSIRIS clearly has multiple opportunities to sample the widespread

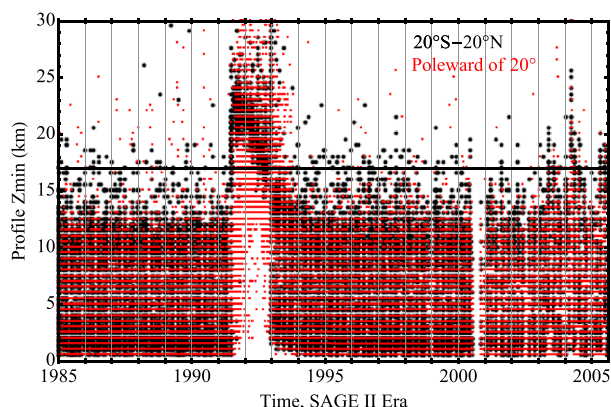


**Figure 11.** Time series of SAGE II profile  $Z_{\text{min}}$  for the instrument's entire record (1 January 1985 to 22 August 2005). Vertical lines at 1 January. Black dots represent profiles equatorward of  $20^{\circ}$  latitude. Red, smaller dots represent profiles poleward of  $20^{\circ}$  latitude. Horizontal line at 17 km marks the typical tropical tropopause altitude [Gettelman et al., 2011].

plume and indeed resolves aerosol enhancements. However, the apparently truncated profiles of Figure 10f suggest that vertical sampling through the plume is reduced (see section 3.2.1).

In summary, even though ground-based lidar, IASI, MLS, and CALIOP revealed Nabro  $\text{SO}_2$  and particles in the stratosphere above 380 K, and up to 19 km in the first 4 days after eruption, OSIRIS's vertical and horizontal sampling at that time showed no signal of a stratospheric perturbation. In the Asian monsoon region, 1 month later, OSIRIS data were characterized by some profiles resolving modest aerosol enhancement layers and others with abnormally high profile termination. A detailed analysis of this issue follows.

### 3. OSIRIS Sampling and Saturation Issues

#### 3.1. Historical Perspective

Satellite limb-sounding instruments operating in the visible to near IR are capable of detecting some optically thin aerosol and cloud layers in the troposphere and stratosphere. The longest legacy of such measurements is maintained by instruments operated in the solar occultation mode, such as Stratospheric Aerosol Measurement II, Stratospheric Aerosol and Gas Experiment (SAGE) I–III (and a few additional instruments not mentioned). These instruments delivered 1 km vertical resolution aerosol extinction profiles between 1978 and 2005. Each instrument's Sun-tracking method and sensitivity are, of course, different. However, they all have a sensitivity limit when the solar transmission is reduced to the point where signal-to-noise is insufficient to retrieve aerosol/cloud extinction. Put simply, when an opaque cloud or aerosol layer (or the hard Earth) occults the Sun, the extinction profile terminates.

In clear-sky conditions, NASA's SAGE II and III could retrieve aerosol extinction down to 4 km above the Earth's surface [e.g., Treffeisen et al., 2006]. Tropospheric clouds are almost always too optically thick for these instruments, causing the profile to terminate at or just above the cloud top [Wang et al., 1995]. Stratospheric aerosols and clouds are also known to cause profile termination above the feature top. In their study of the young Mount Pinatubo aerosol plume in 1991, McCormick and Veiga [1992] referred to this SAGE II feature as the "aerosol cloud top" and found profiles truncating as high as 29 km. In fact, they found that at some point soon after the eruption, a majority of SAGE II's tropical profiles truncated far above its normal profile termination near or below the tropopause. Figure 11 reveals that in the 20 year SAGE II record, the Mount Pinatubo era stands out in this regard. Truncated profiles at the aerosol layer top were a common feature globally and persisted for 3 years.

Aerosol optical thicknesses sufficient to truncate solar-occultation measurements in the stratosphere have other sources in addition to volcanic aerosol plumes. For example, some polar stratospheric clouds (PSCs) [Fromm et al., 1997, 1999; Palm et al., 2005] and stratospheric wildfire smoke plumes can also truncate measurements. Fromm et al. [2005] showed a pair of Polar Ozone and Aerosol Measurement (POAM) III and SAGE II profiles in close proximity—both sampling a stratospheric smoke plume—where SAGE II resolved the smoke layer with a  $0.013 \text{ km}^{-1} 1 \mu\text{m}$  extinction coefficient at 2 km above the tropopause, and POAM III cut off just above this layer. This same paper showed that POAM recorded these so-called "High  $Z_{\text{mins}}$ " (profile termination 3 or more km above the tropopause) in the smoke plume a full 3 weeks after pyrocumulonimbus (pyroCb) smoke injection. Modeling High  $Z_{\text{mins}}$  conditions revealed that POAM II's 780 nm extinction sensitivity limit was  $\sim 0.02 \text{ km}^{-1}$  [Fromm et al., 1999]. Two papers, Wang et al. [1995, 2001] determined that SAGE II had a sensitivity limit of 1020 nm extinction coefficient  $0.02 \text{ km}^{-1}$  and  $0.03 \text{ km}^{-1}$ , respectively. Both of these values, considered for a 1 km deep layer, are close to the definition of "subvisual cirrus" [Sassen et al., 1990].

**Table 2.** Average OSIRIS Profile Termination Versus Tropopause Statistics for 13 June to 13 August<sup>a</sup>

	2010			2011			2012		
	AM	Wlon	Nlat	AM	Wlon	Nlat	AM	Wlon	Nlat
N	950	1504	2301	555	1484	2079	703	1109	1645
OZ <sub>min</sub> (km)	16.34	15.91	14.39	17.98	16.28	14.87	16.17	15.89	14.33
Z <sub>trop</sub> (km)	14.88	13.94	10.87	15.13	13.85	10.73	14.69	13.86	10.97
Delta (km)	+1.46	+1.97	+3.52	+2.85	+2.43	+4.14	+1.48	+2.03	+3.36
Oθ <sub>min</sub> (K)	388.3	388.2	390.5	423.8	394.2	398.9	384.8	386.6	388.2
θ <sub>trop</sub> (K)	370.4	361.3	336.9	370.9	359.5	334.3	369.1	360.0	336.8
Delta (K)	+17.9	+26.9	+53.6	+52.9	+34.7	+64.6	+15.7	+26.6	+51.4

<sup>a</sup>Geographic regions are as follows: 20°N–45°N, 20°E–140°E, for the Asian monsoon (AM); 20°N–45°N, west longitudes only (Wlon); and 45°N–60°N, (Nlat).

The cited studies of volcanic sulfates, pyroCb smoke, and PSCs make clear that if the aerosol-profile data set is taken at face value, potentially significant volumes of stratospheric air will be inferred to be absent of aerosols when in fact quite the opposite is true. In the case of Mount Pinatubo, McCormick and Veiga [1992] employed a proxy extinction value for this unseen atmosphere to deal with the AOD underestimation that contaminated the SAGE II record in this early posteruption phase. Thomason and Peter [2006] filled in aerosol extinction below this so-called “saturation” level with proxy extinction data based on ground-based lidar profiles. Fromm et al. [2005] chose not to inflate the measured POAM III AOD values in the analysis of the young pyroCb plume but rather annotated the aerosol time series to show when these unseen but particularly large-AOD samples were detected. Although such approaches to account for the High Z<sub>min</sub> are necessary, they are unsatisfactory because the cloud/plume that is undetected can exhibit physical properties ranging from a single, geometrically thin layer to a vertically broad or multilayered structure. The cloud/plume can embody an extinction coefficient ranging from the instrument's sensitivity limit up to values representative of visible clouds, spanning multiple orders of magnitude. While the occurrence of a High Z<sub>min</sub> prevents us from providing a quantitative measure of aerosols in the presence of a strong plume, the existence of such events must be accounted for explicitly in any remote-sensing analysis of a young/concentrated aerosol plume in the stratosphere.

### 3.2. OSIRIS Vertical Sampling and Aerosol Sensitivity

The Version 5.07 OSIRIS Optical Spectrograph (OS) 750 nm aerosol data set contains confirmation of the High-Z<sub>min</sub> effect with a deleterious potential regarding interpretation of young/strong stratospheric aerosol plumes. Although OSIRIS's OS operates in limb scatter mode, it is reasonable to expect an analog to the High Z<sub>min</sub> in this data set. Our search of the literature did not uncover any analysis of OSIRIS OS profile termination as a function of cloud optical depth and altitude. However, the OSIRIS Level 2 User Guide for OS data supports the contention of the High-Z<sub>min</sub> effect in the statement: “The instrument cannot meaningfully measure below the upper cloud deck and even under clear sky conditions starts to suffer detector saturation problems at altitudes below 7 km altitude (<http://odin-osiris.usask.ca/sites/default/files/media/pdf/l2dataformat.pdf>).” To assess how well OSIRIS characterizes the aerosol loading in the lower stratosphere, two questions arise: (1) How much of the lowermost stratosphere does OSIRIS typically resolve? and (2) What is the OSIRIS OS cloud/aerosol extinction threshold? We address these questions with an empirical approach.

#### 3.2.1. OSIRIS Minimum Altitude

The OSIRIS-profile terminal altitude is defined as the lowest altitude bin containing a retrieved aerosol extinction coefficient. We evaluate OSIRIS-profile terminal altitude relative to the tropopause, expressed both in terms of geometric height and potential temperature. Tropopause height and potential temperature (Z<sub>trop</sub> and θ<sub>trop</sub>, respectively) are calculated using the pv-based definition (profiles equatorward of 20° latitude are not considered in this analysis). Interpolation in space and time to OSIRIS is performed, using daily National Centers for Environmental Prediction reanalysis data [Kalnay et al., 1996]. Hereafter, the OSIRIS-profile terminal height and θ will be referred to as OZ<sub>min</sub> (km) and Oθ<sub>min</sub> (K), respectively.

We chose 3 years and three geographical regions within which to calculate average OZ<sub>min</sub>, Oθ<sub>min</sub>, Z<sub>trop</sub>, and θ<sub>trop</sub>. The time periods are 13 June to 13 August, for years 2010–2012. The 2 month interval begins on the Nabro volcano eruption date. The 3 years include the Nabro year (2011) and surrounding years with no

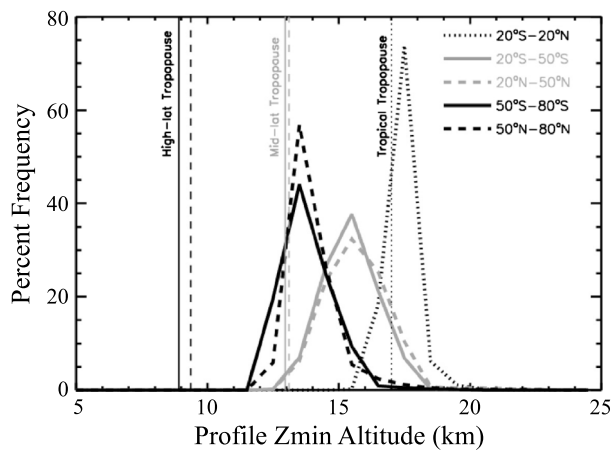


**Figure 12.** Histogram of OSIRIS profile  $Z_{\text{min}}$ . Frequency bins are 1 km wide. Five zones covering the Earth to the 80<sup>th</sup> parallel are defined in the legend. Every OSIRIS profile through 2012 is included. Vertical bars indicate the average tropopause height in each zone. The dynamical tropopause definition (see text for details) is used outside the tropics. The tropical tropopause is taken to be 17 km [Gettelman *et al.*, 2011].

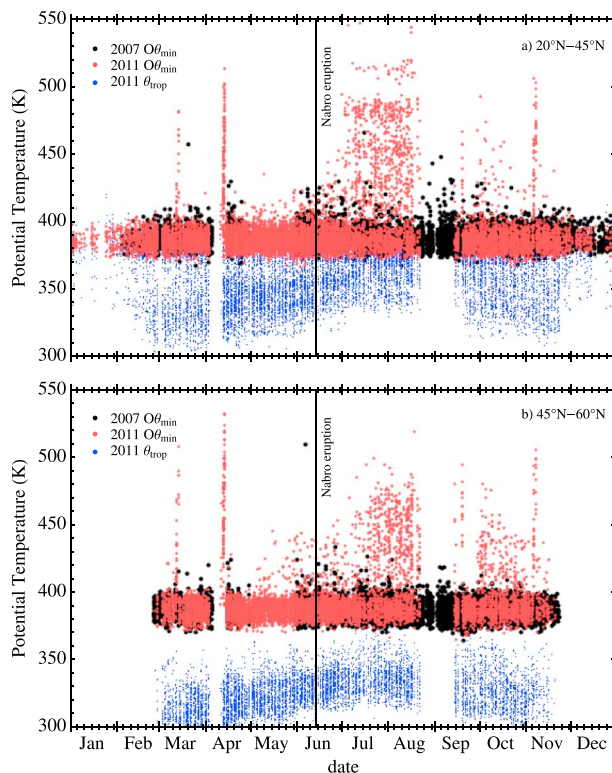
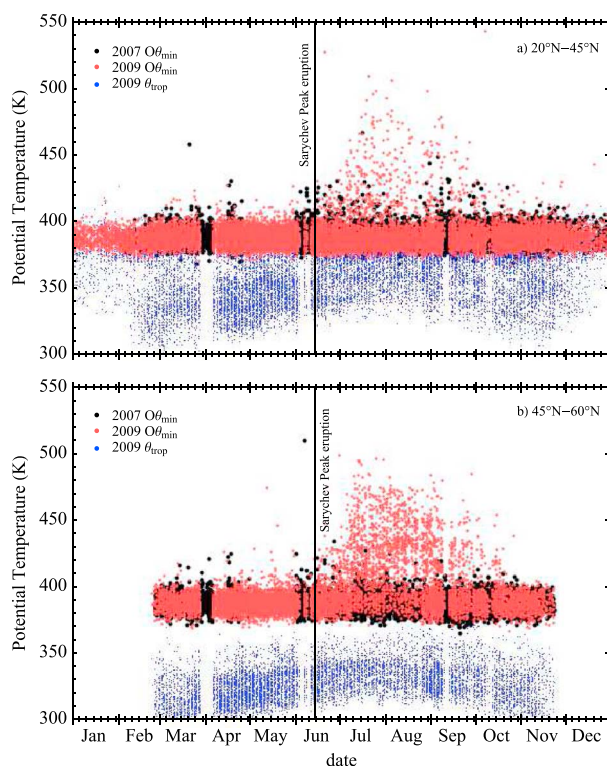


**Figure 13.**  $O\theta_{\text{min}}$  and  $\theta_{\text{trop}}$  for each OSIRIS profile in 2007 and 2011, in two latitude belts, (a) 20°N–25°N and (b) 45°N–60°N. 2011 data are plotted with smaller dots. Black (red) dots are  $O\theta_{\text{min}}$  for 2007 (2011). Blue dots are  $\theta_{\text{trop}}$  for 2011. Note the ~20 day OSIRIS data gap in August and September (also reflected as a gap in Figure 4 of B12).

significant stratospheric volcanic impact. The geographical zones are 1. 20°N–45°N, 20°E–140°E, for the Asian monsoon (AM); 2. 20°N–45°N, west longitudes (Wlon); and 3. 45°N–60°N (Nlat).

Table 2 contains averages for  $OZ_{\text{min}}$ ,  $O\theta_{\text{min}}$ ,  $Z_{\text{trop}}$ , and  $\theta_{\text{trop}}$  for each year and geographical zone. The 3 year average tropopause height and  $\theta$  in the AM (where the tropopause is high relative to the other zones) is approximately 15 km and 370 K, respectively. Considering this result, it is evident that the 380 K threshold used elsewhere herein is a more restrictive criterion for the stratosphere. In the AM zone for the two nonvolcanic years, OSIRIS typically probed down to just above 16 km, ~1.4–1.7 km higher than the tropopause. In terms of  $\theta$ , OSIRIS terminated at ~387 K, 18 K above the tropopause. In the Wlon zone,  $OZ_{\text{min}}$  was typically just below 16 km but slightly higher with respect to the tropopause (~2 km) than in the AM. In terms of  $\theta$ , OSIRIS typically terminated ~387 K, ~27 K above the tropopause in 2010 and 2012. In the Nabro season,  $OZ_{\text{min}}$  and  $O\theta_{\text{min}}$  were considerably higher in the AM both absolutely and with respect to the tropopause. From these results, we see that in an unperturbed stratosphere in the 20°N–45°N zones that OSIRIS typically terminates not only above the tropopause but also above 380 K as well. In perturbed conditions such as the Nabro summer 2011, this measurement offset rises considerably.

Even the stratosphere above 380 K was systematically undersampled in the AM in summer 2011 vis-à-vis the two clean years (not shown in Table 2). The proportion of OSIRIS AM profiles probing below 400 K is 48% in 2011, compared to 95% and 98% in 2010 and 2012, respectively. Moreover, the onset of the reduced sampling in 2011 is approximately the Nabro eruption date; the proportion of OSIRIS AM profiles terminating below 400 K in the two months preceding 12 June 2011 is 95%, consistent with the prior and following summers. Given that the likely reason for OSIRIS-profile termination well into the stratosphere is the presence of aerosol plumes, it is evident that not accounting for the “missing” aerosol will corrupt the analysis of stratospheric volcanic impact.



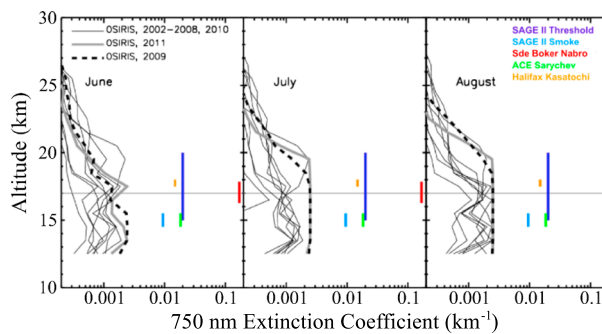
**Figure 14.** Same as Figure 13 but comparing 2009 (red and blue dots) with 2007. Here the vertical bar at 13 June signifies the Sarychev Peak eruption, coincidentally at about the same date as Nabro's eruption.

Table 2 contains information regarding OSIRIS profile termination at middle and high latitudes as well. Here we see that even though the tropopause is considerably lower than in the lower latitudes of the AM and Wlon zones, OSIRIS profiles typically terminate higher on a tropopause-relative basis: over 3 km in 2010 and 2012. Interestingly, Table 2 shows that, in terms of  $\theta$ , OSIRIS Nlat profile termination is typically higher than in lower latitudes. Thus, in summary, it appears that OSIRIS vertical sampling of the lower stratosphere globally is incomplete and, in a poleward direction, is increasingly biased. The generality of this condition is illustrated in Figure 12. Here the entire OSIRIS data set between 2001 and 2012 was subjected to a histogram analysis of  $OZ_{\min}$  and  $Z_{\text{trop}}$ . Five latitude zones spanning 80°S to 80°N reveal  $OZ_{\min}$  tendencies in the tropics, low-latitude extratropics, and high latitudes. Figure 12 shows that tropical  $OZ_{\min}$  mode is  $\sim 0.5$  km above the tropopause, extratropical  $OZ_{\min} \sim 2.5$  km above, and high-latitude  $OZ_{\min} \sim 4.5$  km above. Outside the tropics, the proportion of OSIRIS profiles probing to the tropopause is between 0 and 5%.

### 3.2.2. OSIRIS High-Zmin Effect

A time-series analysis of OSIRIS Zmin brings these issues into focus. Figure 13 shows individual-profile  $O\theta_{\min}$  for two calendar years: 2007 (a year with no documented volcanic stratospheric plume) and 2011, and  $\theta_{\text{trop}}$  for 2011. The latitude belt subsets in Figure 13 are as defined for Table 2, 20°–45°N (Figure 13a) and 45°–60°N (Figure 13b). Aside from a few spurious daily spikes (e.g., in mid-March and mid-April), the temporal pattern of  $O\theta_{\min}$  in 2011 shows a narrow range in spring and autumn in both 2007 and 2011, between 370 and 400 K.  $\theta_{\text{trop}}$  is offset below  $O\theta_{\min}$  throughout the period in both latitude zones. In the summer months of both years, in both latitude belts, there is an increased occurrence of  $O\theta_{\min}$  above 400 K—an OSIRIS manifestation of the High Zmin. However, in 2011 the High-Zmin occurrence frequency and top  $\theta$  are much greater than in 2007. The onset in 2011 was around the date of the Nabro eruption and persisted into autumn.

Figure 14 presents a corresponding analysis of 2007 and 2009, during the latter of which the Sarychev Peak volcano in the Kurile Island chain (48.1°N, 153°E) erupted, directly injecting SO<sub>2</sub> and aerosols into the stratosphere [H10; K11; O12; Rybin *et al.*, 2011; Carn and Lopez, 2011; Doeringer *et al.*, 2012]. According to Rybin *et al.* [2011], Sarychev Peak erupted explosively between 12 and 16 June. The first three of the papers cited above involved OSIRIS aerosol data in their analyses. As mentioned in section 1, the authors contended with a low bias in OSIRIS AOD and a temporal offset in peak OSIRIS AOD (OSIRIS peaking later). For instance, K11 found that OSIRIS AOD was an order of magnitude smaller than model simulations (the same bias reported by K10 for Kasatochi). H10 found that OSIRIS AOD peaked about 1 month later than the model. These papers each discussed the OSIRIS discrepancies and attempted reconciliation but could not resolve the issue. H10 consequently concluded that their model needed refinements in its gas-particle nucleation scheme. A similar conclusion was reached by Heard *et al.* [2012] who encountered the same discrepancies in an analysis of both Kasatochi and Sarychev with the UK Met Office's Numerical Atmospheric-dispersion Modeling Environment and OSIRIS data.



**Figure 15.** Profiles of global maximum OSIRIS 750 nm aerosol extinction coefficient for three individual northern summer months (June, left; July, center; August, right). Thin gray lines are for the years identified in the upper left legend. Thick gray line, 2011. Thick, black, dashed line, 2009. Horizontal line at 17 km represents the typical tropical tropopause [Gettelman et al., 2011]. Colored annotations show non-OSIRIS observations of stratospheric aerosol extinction coefficient, all converted to 750 nm. “SAGE II Threshold” is from Wang et al. [1995]. “SAGE II Smoke” is from Figure 15 of Fromm et al. [2005]. “ACE Sarychev” from Figure 7b of Doeringer et al. [2012]. “Halifax Kasatochi” from Figure 2 of Bitar et al. [2010]. Conversion to 750 nm extinction is by linear interpolation between 1020 and 525 nm in the case of SAGE II data. For others, we use an Angström exponent = 1.

Mount Pinatubo aerosols [McCormick and Veiga, 1992]. PSCs [Poole and Pitts, 1994] and smoke plumes [Siddaway and Petelina, 2011] have been observed at altitudes above 20 km. We represent such aerosol features, in terms of observed 750 nm aerosol extinction coefficient in Figure 15, which also illustrates profiles of maximum OSIRIS 750 nm aerosol extinction coefficient. The profiles shown in Figure 15 show the maximum extinction coefficient reported by OSIRIS at 750 nm for all northern latitudes for the summer months June–August. The years of the Sarychev Peak (2009) and Nabro (2011) plumes are highlighted; the other years between 2002 and 2011 are shown individually with thin lines. Since the Figure 15 analysis is for all latitudes, it includes a line at 17 km to mark the typical altitude for the globe’s highest tropopause, which occurs in the tropics [Gettelman et al., 2011].

We see in July and August 2009 and 2011, a constant extinction maximum of  $\sim 0.0025 \text{ km}^{-1}$  from  $\sim 14$  to 20 km. Since altitudes above 17 km are considered stratospheric globally, this constant extinction maximum certainly penetrates into the stratosphere. Above this feature, maximum extinction declines by roughly an order of magnitude near 25 km. The OSIRIS maximum extinction pattern suggests an empirical stratospheric aerosol sensitivity limit of  $\sim 0.0025 \text{ km}^{-1}$ . The color-coded bars in Figure 15 show independent aerosol extinction coefficient retrievals from ground-based lidar and satellite solar occultation at their reported altitude (details in Figure 15 caption). Despite the range of altitudes, the non-OSIRIS observations were all at  $\theta > 380$  K. Also shown is the reported SAGE II extinction threshold at 750 nm. The observations of volcanic sulfate and forest fire smoke extinction in Figure 15 illustrate the routine occurrence of aerosol plume loading beyond the apparent OSIRIS sensitivity limit. That plumes such as these occur in proximity to OSIRIS High Zmins is demonstrated next.

### 3.2.4. OSIRIS Nabro High-Zmin Example

In section 2.5 we showed (Figure 10f) several OSIRIS profiles truncated abnormally high above the tropopause in mid-July. Here we present an example of an OSIRIS High Zmin in proximity to height-resolved Nabro aerosol layers that exceed the empirical OSIRIS extinction threshold. Figure 16 combines an OSIRIS profile near Hawaii on 21 July 2011 (OSIRIS scan 56768000,  $20.92^\circ\text{N}$ ,  $157.80^\circ\text{W}$ ) 5 weeks after the Nabro eruption sequence, and CALIOP and ground-based lidar profiles near/at Mauna Loa. The Mauna Loa lidar operated by NOAA is part of the Network for the Detection of Atmospheric Composition Change (<http://ndacc-lidar.org/>). See Figure 17 for the locations of the three instruments’ measurements.

Although not shown, CALIOP and Mauna Loa lidar data reveal that the aged Nabro layer was widespread, homogeneous, and persistent at this time. We selected CALIOP measurements within  $0.5^\circ$  latitude of Mauna

None of these papers explored the potential effect of High Zmins in the OSIRIS aerosol data set. Figure 14a shows that after the mid-June direct stratospheric injection by Sarychev Peak, OSIRIS incurred a similar onset of High Zmins as it did in the Nabro summer. The impact is seen to be much stronger in northern latitudes, closer to the volcanic source. However, in both latitude belts the increase in High Zmins is substantial and persists into autumn. As discussed above, a large, systematic truncation of aerosol profiles will introduce a potentially strong bias to average AOD. Next we will explore this potential.

### 3.2.3. OSIRIS Extinction Threshold

It is essential to characterize the range of 750 nm aerosol extinction coefficient that can occur in the lower stratosphere in order assess the OSIRIS sensitivity limit. As discussed previously, both stratospheric aerosol plumes and clouds can occupy the measurement volume. We know that altitudes as high as 35 km were impacted by

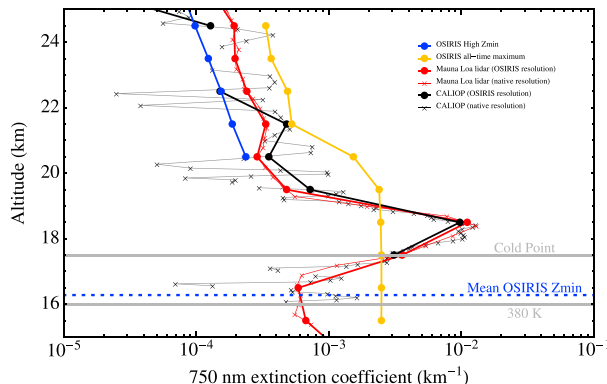


**Figure 16.** Aerosol extinction coefficient at 750 nm on 21 July 2011 near Hawaii (see Figure 17). Mauna Loa ( $19.5^{\circ}\text{N}$ ,  $155.6^{\circ}\text{W}$ ), red; OSIRIS ( $20.9^{\circ}\text{N}$ ,  $157.8^{\circ}\text{W}$ ), blue; and CALIOP, black. CALIOP data are averaged along its orbit between  $19^{\circ}\text{N}$  and  $20^{\circ}\text{N}$ . Shown for Mauna Loa and CALIOP are both the native altitude resolution and a linear interpolation to OSIRIS altitudes. Blue dotted line: average  $\text{OZ}_{\text{min}}$  from Table 2, 2011, Wlon. Horizontal gray bars are at altitude of OSIRIS-colocated cold point, and  $\theta = 380 \text{ K}$ . Gold line is the all-time OSIRIS extinction maximum.

AOD. AOD was calculated by integrating extinction coefficient above 380 K. OSIRIS profile locations with AOD color coded identically to CALIOP are plotted as polygons. The map shows that CALIOP AOD was much greater than the OSIRIS value over a north-south distance greater than 1000 km. The largest  $> 380 \text{ K}$  AOD in the 2001–2012 global OSIRIS record is 0.021, which according to the color scale in Figure 17 is considerably less than many of the CALIOP observations in this 5 week old plume.

This example illustrates environmental conditions that would reasonably cause OSIRIS High Zmins. The empirical fact that OSIRIS is insensitive to aerosol abundances manifesting 750 nm extinction coefficient

beyond  $\sim 0.0025 \text{ km}^{-1}$  indicates that OSIRIS can, at best, resolve lowermost stratospheric aerosol enhancements within roughly an order of magnitude of background ( $\sim 10^{-4} \text{ km}^{-1}$ ). Roughly another order of magnitude lies between the OSIRIS and the SAGE sensitivity limits. Stratospheric volumes of air with aerosol abundances beyond the OSIRIS sensitivity limit will be unrepresented in any analysis of such a plume. The empirical maximum-extinction profile also suggests that for a plume below  $\sim 20 \text{ km}$ , OSIRIS will only fully resolve that plume if it embodies 750 nm extinction coefficients less than  $0.0025 \text{ km}^{-1}$  and resides wholly above 380 K. From a geographic perspective, this implies that for optically thicker plumes, OSIRIS will only resolve the upper vertical bound and horizontal plume periphery. The two discrepancies with which the Sarychev Peak papers struggled, and the conclusion that Nabro aerosols first showed up in the stratosphere on 1 July 2011 [B12] more than

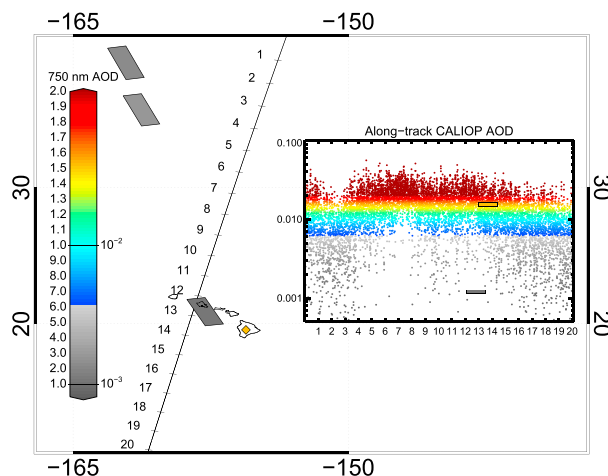


**Figure 17.** Map of Hawaii, showing stratospheric AOD from Mauna Loa lidar (filled diamond on Hawaii), three OSIRIS profile locations (gray polygons) and a CALIOP segment on 21 July 2011. Inset shows dots for CALIOP AOD and bars (at the nearest CALIOP measurement location) for Mauna Loa lidar and OSIRIS AOD nearest to Mauna Loa. Symbols for the three measurement types on the map and inset are colored according to the AOD scale (coefficient on the left side and order of magnitude on the right side of the color bar). The OSIRIS profile over Hawaii ( $20.9^{\circ}\text{N}$ ,  $157.8^{\circ}\text{W}$ ) is the High-Zmin case illustrated in Figure 16.

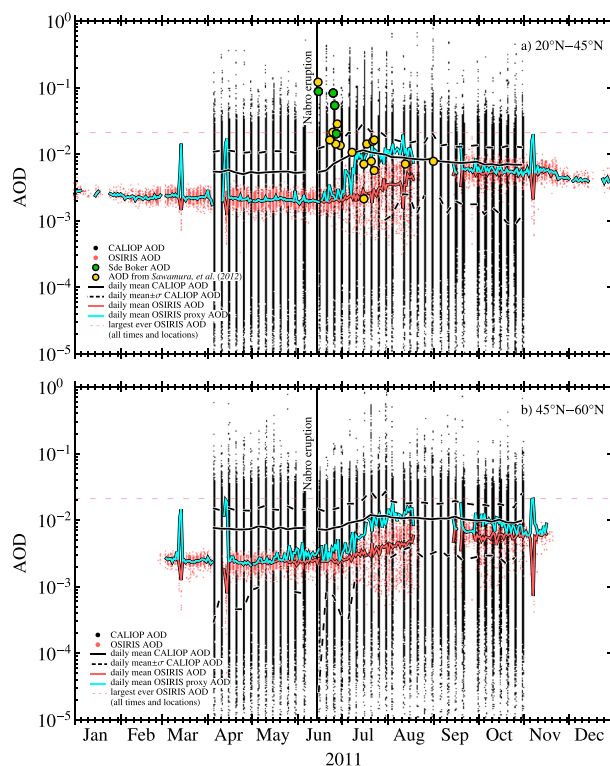


**Figure 18.** Time series of OSIRIS and CALIOP stratospheric AOD (i.e., extinction integrated above  $\theta = 380$  K) in the two latitude belts defined in Table 2, for 2011: (a)  $20^{\circ}\text{N}$ – $45^{\circ}\text{N}$  and (b)  $45^{\circ}\text{N}$ – $60^{\circ}\text{N}$ . Red dots, OSIRIS individual-profile AOD; red solid line, daily average; red dashed line, OSIRIS data set maximum AOD; blue line, daily average OSIRIS AOD where a proxy AOD = 0.02 is added to individual High-Zmin profiles (profiles truncated more than 2 km above  $\theta = 380$  K); black dots, CALIOP profile AOD (see text for details of calculation); black line, daily average; black dashed line,  $\pm 1$  standard deviation ( $\sigma$ ); gold dots, AOD from cited publication; green dots, Sde Boker lidar. Note that the lower CALIOP  $\sigma$  envelope before mid-July is negative in Figure 18a and is not represented on a logarithmic scale.

zones defined in Table 2 and shown in Figures 13 and 14. Figure 18 also shows individual-profile AOD (red dots), the daily average AOD (red line), and the daily average proxy-augmented AOD (blue line).

The OSIRIS individual-profile AODs show a narrow spread prior to the Nabro eruption and spread widely soon thereafter. Peak AOD increases with respect to pre-Nabro, but some values are significantly smaller than the pre-Nabro minimum. From about September onward the AOD range retightens in a pattern consistent with gradual aerosol mass loading decay. The daily average only starts to increase posteruption after an approximate 2 week lag and reaches a maximum after the month-long data gap between August and September. The proxy-augmented AOD manifests a very different pattern: earlier plume onset and an earlier peak in daily average values. This of course occurs in the period with the large frequency of High Zmins (see Figures 13 and 14). Note that the timing of the peak in the average AOD will always be related to an instrument's maximum measurable AOD, with the period between injection and peak average AOD becoming longer as the maximum individual AOD becomes smaller. This is simply the result of only being able to measure AODs once the plume has dispersed sufficiently to avoid terminating the profile too high. By using a proxy AOD, we can to some extent ameliorate this unphysical delay but we cannot eliminate it.

We use nighttime CALIOP Level 1 data containing 532 nm total attenuated backscatter coefficients ( $\beta'$ ) to form a comparative Nabro AOD time series. Daytime profiles are found to be too noisy to accurately identify the weak backscattering signals associated with aging volcanic aerosols. Details of our method for conversion of 532 nm backscatter to 750 nm extinction and AOD is contained in the supporting information. The

2 weeks after the volcanic eruption, are consistent with the plume biasing identified here.

### 3.2.5. Treatment for Nabro and Sarychev Peak Discrepancies

There appears to be no obvious analytical remedy for the general undersampling of the lower stratosphere by OSIRIS as illustrated in Figure 12. However, measures similar to those taken in prior papers [e.g., McCormick and Veiga, 1992] dealing with “aerosol cloud tops,” profile “saturation,” or “High Zmins” can enable a new interpretation of plumes that trigger High Zmins, such as Sarychev Peak and Nabro. For example, we use a proxy approach for dealing with High Zmins in Figures 18 and 19. By its nature, the proxy is arbitrary—there is no knowledge of the underlying plume. However, we obtain guidance from our analysis of OSIRIS maximum extinction compared to independent observations (e.g., Figure 16) and the approach of McCormick and Veiga [1992]; they extrapolated the SAGE II terminal-altitude extinction to the tropopause before integrating for AOD. These insights led us to experiment with proxies: constants to be added to the OSIRIS AOD for profiles with a terminal altitude 2 or more kilometers higher than  $\theta = 380$  K. We represent those experiments by showing the results with proxy = 0.02, which approximates subvisual cirrus AOD. Figure 18 shows 2011 OSIRIS AOD above 380 K, which is the same lower boundary used by K10, K11, H10, and B12 for the same two latitude

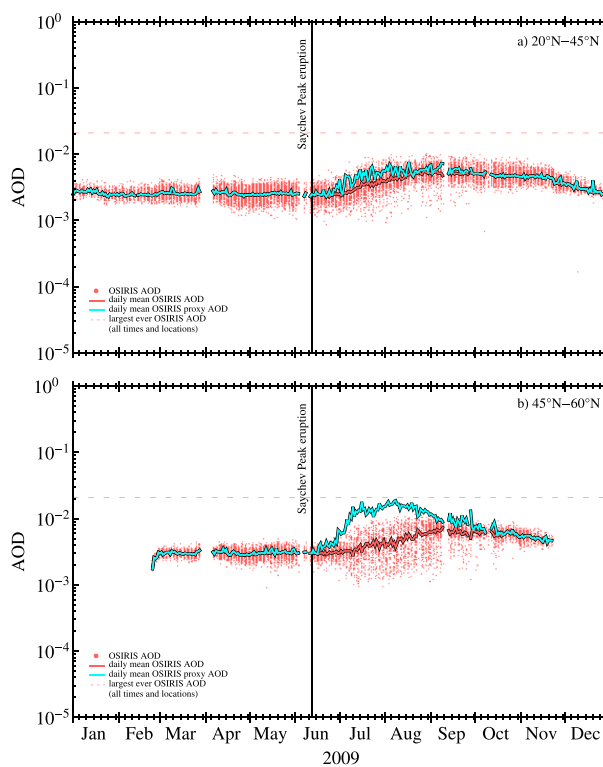


**Figure 19.** Similar to Figure 17 but with only the OSIRIS component, and for 2009 (Sarychev Peak eruption) instead of 2011.

age OSIRIS into greater agreement with CALIOP in terms of both magnitude and timing AOD increase. A similar comparative pattern is evident in the 45°N–60°N zone (Figure 18b).

Annotated on Figure 18a are additional measurements of AOD from ground-based lidar. Many of the observations are taken from Table 2 of *Sawamura et al. [2012]*. In addition to these, we show 750 nm AOD from Sde Boker immediately after the eruption onset. These AOD points make clear that stratospheric aerosol mass right after Nabro's eruption was within the range of CALIOP AOD (albeit far greater than  $1\sigma$ ) but surpassed the maximum all-time OSIRIS AOD. It can be seen from the additional data plotted in Figure 18a that the proxy modification of the OSIRIS High Zmins improves consistency among data sets. The space- and ground-based lidar data show clearly that Nabro's stratospheric plume was immediate and embodied aerosol abundance well beyond the OSIRIS sensitivity limit. The addition of the proxy reconstitutes the OSIRIS AOD time series in both latitude belts, one comprising the Asian monsoon and the poleward latitude zone outside monsoon influence. We deduce from this analysis that OSIRIS biasing of the Nabro plume was incidental to the Asian monsoon influence, and by extension the Nabro stratospheric plume was incidental to the monsoon circulation. The immediate posteruption large-AOD observations at Sde Boker also shed light on the inherent weakness of representing the evolution of young, concentrated volcanic plumes by averaging aerosol abundance over large spatial and temporal bounds, such as the daily averages shown in Figure 18 and similar attempts in the various papers cited herein.

These Nabro-event results are completely analogous with those in the Sarychev Peak year (Figure 19). Figure 19 contains only the OSIRIS component but is otherwise identical to Figure 18. Here the proxy-augmented AOD is most pronounced in the 45°N–60°N belt, within which the volcano is situated. The proxy signals an earlier aerosol onset, a more rapid growth phase, a larger maximum AOD, and earlier peak AOD. The discrepancies reported in the above-mentioned Sarychev Peak papers are partially ameliorated by this simple proxy experiment. However, since our choice for the proxy value is less than some AOD observations (e.g., see the examples in Figure 18a) and near the OSIRIS historical AOD maximum, it is likely still biased low. This represents a fundamental limitation of any such measurement.

results of this calculation are presented in Figure 18. The spread of individual CALIOP AOD is relatively large. Hence, we summarize the time series by calculating a daily average and standard deviation ( $\sigma$ ). In order to keep the amount of computations tenable, we use CALIOP data from approximately every fifth day over the 5 April to 30 October (CALIOP has data gaps near the beginning of August and end of September, causing some sequential dates in the time series to be longer or shorter than 5 days apart). For the 20°N–45°N zone in Figure 18a, we see a pre-Nabro positive offset between CALIOP and OSIRIS, with OSIRIS AOD straddling the CALIOP  $1\sigma$  line. After the Nabro eruption, CALIOP AOD increases immediately after a 10 day data gap and reaches a peak in mid-July, while OSIRIS AOD was still increasing. This initial lag in OSIRIS AOD is attributed to the large occurrence of High Zmins (Figure 13a). In September and October, after the incidence of OSIRIS High Zmins is diminished, CALIOP and OSIRIS daily average AOD converges. The proxy AOD pattern brings daily aver-

As discussed above, there is apparently no obvious remedy available to the user of OSIRIS aerosol data for the incomplete sampling of the lowermost stratosphere. This is particularly a problem at middle- to high-northern latitudes where the Sarychev Peak plume was strongest. The proxy does not shed light on this. However, the proxy applied to OSIRIS High-Zmin profiles does provide a reasonable signal of an earlier plume detection and peak loading.

#### 4. Summary and Conclusions

The eruption of Nabro volcano beginning on 12 June 2011 was indisputably sudden and violent, considering the classic TIR-based evidence presented here and in V13. The detailed TIR time series (Figure 1) reveals that the volcano continuously generated opaque volcanic-convective cloud tops high into the troposphere through 16 June. On 12–13 June the BT-determined cloud top reached the cold point altitude. Ground-based lidar at Sde Boker, Israel, detected stratospheric aerosol on 14 June, within 1 day of the first deep injection. Isentropic trajectories showed that these particles conformed to the location/time of the early cold cloud top data. Stratospheric MLS SO<sub>2</sub>, also measured on 14 June, was traced to the volcano on the first full eruption day via back trajectory. A variety of stratospheric aerosol and SO<sub>2</sub> layers (Table 1) were also traced to Nabro on 13 June. In each instance, the reported heights matched or exceeded the BT-inferred injection altitude. Again, on 16 June, cloud top BT reached relative minima suggestive of a deep injection. Simultaneous MLS SO<sub>2</sub> and CALIOP aerosol measurements early on 18 June, at reporting heights exceeding the 16 June BT estimates, traced to the volcano on that day. Hence, the geostationary TIR data provide a qualitative, generally low-biased view of these two separate UTLS injections at Nabro.

IASI SO<sub>2</sub> height retrievals, available twice per day, resolved two incipient mesoscale-size (i.e., on the order of 500 km length) stratospheric SO<sub>2</sub> plumes, on 13 and 17 June. These, together with the Sde Boker, MLS, and CALIOP data showed that the Nabro gases and particles rapidly reached altitudes between 17 and 19 km, up to 435 K in terms of potential temperature.

IASI SO<sub>2</sub> data permitted us to follow the two deep-injection plumes out to 18 June, where they occupied distinct locations over the Middle East to East Asia (Figures 2–7). During that period, OSIRIS native sampling was seen to provide very few potential intercepts with the stratospheric plume. Neither the potential intercepts nor any other profile between northeast Africa and East Asia detected an apparent increase in stratospheric aerosol. However, it was evident from these OSIRIS aerosol profiles (Figure 10) that an altitude range up to 4 km above the tropopause was not sampled. Mateshvili *et al.* [2013], who used OSIRIS data to compare with ground-based profile retrievals of Nabro aerosols in the South Caucasus region, encountered the same limitations of horizontal/vertical OSIRIS sampling. Thus, a combination of sparse horizontal/temporal sampling and incomplete stratospheric sampling during the early days of the stratospheric plume—made manifest by IASI—is a viable explanation for the delayed increase of OSIRIS AOD reported by B12.

We showed in our survey of the literature and analysis of OSIRIS data that the post-Nabro OSIRIS pattern of stratospheric AOD [B12] was logically identical to that reported after the Sarychev Peak eruption in 2009. Three papers on the Sarychev Peak event [H10, K11, O12]—known to have involved direct stratospheric injections—revealed that the OSIRIS AOD-increase interval was delayed with respect to other observations and models and that the peak AOD was biased low. Hence, the Nabro and the Sarychev Peak cases were explored in depth and in analogous form herein.

We found that OSIRIS aerosol profiles, like other limb-scan aerosol data before them, exhibit a response to strong aerosol loading with a phenomenon we called a High Zmin, which is an unusually high termination of measurements above a strong aerosol feature. We also found that the maximum 750 nm aerosol extinction coefficient in the entire OSIRIS aerosol archive through 2012 is  $\sim 0.0025 \text{ km}^{-1}$ . Hence, presumably stronger aerosol features would not be resolvable, and their presence would not be represented in the OSIRIS data set. These High Zmins were in abundance after both Sarychev Peak's and Nabro's eruptions (Figures 13 and 14). A single example of a High Zmin 5 weeks after Nabro, in proximity to CALIOP and ground-based lidar (at Mauna Loa), demonstrated extinctions and AOD far beyond the OSIRIS-observed maxima (Figures 16 and 17).

We explored a treatment for the High Zmin; a proxy AOD addition akin to those applied to the SAGE II data set for the Mount Pinatubo aftermath. Our proxy was applied to the data collected during the Sarychev

Peak and Nabro summers. The proxy-augmented OSIRIS data shortened the onset-to-peak AOD period considerably, bringing these data into closer conformity with the previously reported observations and model simulations. The larger peak AOD (versus the unaugmented OSIRIS data), the shorter posteruption lag, and the more rapid AOD buildup all provide a viable explanation for the discrepancies discussed by H10, K10, K11, and O12—one that also applies to the Nabro event. We conclude that the Nabro stratospheric injections of SO<sub>2</sub> and sulfates were underrepresented, as were those in the case of Kasatochi and Sarychev Peak. Moreover, we find that B12's alternate, unproven vertical transport mechanism (direct, efficient ascent of volcanic material through the tropopause via the Asian monsoon circulation and convection) is not needed to explain the temporal evolution of OSIRIS AOD. This is consistent with other direct-stratospheric volcanic cases involving OSIRIS data. Our results can also be used to motivate a reassessment of the conclusions of H10, K10, K11, and O12. For instance, H10, in constraining their transport-chemistry model to OSIRIS aerosol observations, concluded that the model's aerosol nucleation scheme was misrepresenting sulfate aerosol nucleation and growth. We suggest that fuller accounting of OSIRIS aerosol sampling and sensitivity limitations will give a more accurate view of strong, evolving stratospheric aerosol plumes.

### Acknowledgments

We thank Richard Bankert for assistance with Meteosat TIR data acquisition and Mike Pavoloni for helpful discussion of Nabro's eruption altitude. John Barnes provided the Mauna Loa lidar data. Lubna Bitar provided Dalhousie University lidar extinction data. Arnon Karnieli is the principal investigator of Sde Boker's MPL and made these data available. We are grateful for the diligent efforts of three reviewers and thoughtful handling of this paper by the editors. Radiosonde data were gotten from University of Wyoming College of Engineering, <http://weather.uwyo.edu/upperair/sounding.html>. E.C. and R.G.G. acknowledge funding from the UK Natural Environment Research Council (NERC) National Centre for Earth Observation, the NERC Centre for the Observation and Modelling of Earthquakes, Volcanoes and Tectonics, and the NERC VANAHEIM project NE/1015592/1.

### References

- Bitar, L., T. J. Duck, N. I. Kristiansen, A. Stohl, and S. Beauchamp (2010), Lidar observations of Kasatochi volcano aerosols in the troposphere and stratosphere, *J. Geophys. Res.*, 115, D00L13, doi:10.1029/2009JD013650.
- Bourassa, A. E., D. A. Degenstein, B. J. Elash, and E. J. Llewellyn (2010), Evolution of the stratospheric aerosol enhancement following the eruptions of Okmok and Kasatochi: Odin-OSIRIS measurements, *J. Geophys. Res.*, 115, D00L03, doi:10.1029/2009JD013274.
- Bourassa, A. E., A. Robock, W. J. Randel, T. Deshler, L. A. Rieger, N. D. Lloyd, E. J. Llewellyn, and D. A. Degenstein (2012), Large volcanic aerosol load in the stratosphere linked to Asian monsoon transport, *Science*, 337(6090), 78–81, doi:10.1126/science.1219371.
- Bourassa, A. E., A. Robock, W. J. Randel, T. Deshler, L. A. Rieger, N. D. Lloyd, E. J. Llewellyn, and D. A. Degenstein (2013), Response to comments on "Large volcanic aerosol load in the stratosphere linked to Asian monsoon transport", *Science*, 339(6120), 647, doi:10.1126/science.1227961.
- Campbell, J. R., K. Sassen, and E. J. Welton (2008), Elevated cloud and aerosol layer retrievals from Micropulse Lidar Signal Profiles, *J. Atmos. Oceanic Technol.*, 25(5), 685–700, doi:10.1175/2007JTECHA1034.1.
- Carbone, E., R. Grainger, J. Walker, A. Dudhia, and R. Siddans (2012), A new scheme for sulphur dioxide retrieval from IASI measurements: Application to the Eyjafjallajökull eruption of April and May 2010, *Atmos. Chem. Phys.*, 12(23), 11,417–11,434, doi:10.5194/acp-12-11417-2012.
- Carn, S. A., and T. M. Lopez (2011), Opportunistic validation of sulfur dioxide in the Sarychev Peak volcanic eruption cloud, *Atmos. Meas. Tech.*, 4(9), 1705–1712, doi:10.5194/amt-4-1705-2011.
- Clarisse, L., M. D. Fromm, Y. Ngadi, L. Emmons, C. Clerbaux, D. Hurtmans, and P.-F. Coheur (2011), Intercontinental transport of anthropogenic sulfur dioxide and other pollutants: An infrared remote sensing case study, *Geophys. Res. Lett.*, 38, L19806, doi:10.1029/2011GL048976.
- Clarisse, L., P.-F. Coheur, N. Theys, D. Hurtmans, and C. Clerbaux (2014), The 2011 Nabro eruption, a SO<sub>2</sub> plume height analysis using IASI measurements, *Atmos. Chem. Phys.*, 14, 3095–3111, doi:10.5194/acp-14-3095-2014.
- Dee, D. P., et al. (2011), The ERA-Interim reanalysis: Configuration and performance of the data assimilation system, *Q. J. R. Meteorolog. Soc.*, 137(656), 553–597, doi:10.1002/qj.828.
- Doeringer, D., A. Eldering, C. D. Boone, G. González Abad, and P. F. Bernath (2012), Observation of sulfate aerosols and SO<sub>2</sub> from the Sarychev volcanic eruption using data from the atmospheric chemistry experiment (ACE), *J. Geophys. Res.*, 117, D03203, doi:10.1029/2011JD016556.
- Draxler, R. R., and G. D. Rolph (2013), *HYSPLIT (Hybrid Single-Particle Lagrangian Integrated Trajectory) Model Access via NOAA ARL READY Website*, NOAA Air Resour. Lab., College Park, Md. [Available at <http://www.arl.noaa.gov/HYSPLIT.php>.]
- Fee, D., A. Steffke, and M. Garces (2010), Characterization of the 2008 Kasatochi and Okmok eruptions using remote infrasound arrays, *J. Geophys. Res.*, 115, D00L10, doi:10.1029/2009JD013621.
- Fromm, M. D., J. D. Lumpe, R. M. Bevilacqua, E. P. Shettle, J. Hornstein, S. T. Massie, and K. H. Fricke (1997), Observations of Antarctic polar stratospheric clouds by POAM II: 1994–1996, *J. Geophys. Res.*, 102(D19), 23,659–23,672, doi:10.1029/97JD00794.
- Fromm, M. D., R. M. Bevilacqua, J. Hornstein, E. P. Shettle, K. Hoppel, and J. D. Lumpe (1999), An analysis of polar ozone and aerosol measurement (POAM) II Arctic polar stratospheric cloud observations, 1993–1996, *J. Geophys. Res.*, 104(D20), 24,341–24,358, doi:10.1029/1999JD900273.
- Fromm, M. D., R. M. Bevilacqua, R. Servranckx, J. Rosen, J. P. Thayer, J. Herman, and D. Larko (2005), Pyro-cumulonimbus injection of smoke to the stratosphere: Observations and impact of a super blowup in northwestern Canada on 3–4 August 1998, *J. Geophys. Res.*, 110, D08205, doi:10.1029/2004JD005350.
- Fromm, M. D., G. Nedoluha, and Z. Charvat (2013), Comment on "Large volcanic aerosol load in the stratosphere linked to Asian monsoon transport", *Science*, 339(6120), 647, doi:10.1126/science.1228605.
- Gettelman, A., P. Hoor, L. L. Pan, W. J. Randel, M. I. Hegglin, and T. Birner (2011), The extratropical upper troposphere and lower stratosphere, *Rev. Geophys.*, 49, RG00035, doi:10.1029/2011RG000355.
- Hamada, A., and N. Nishi (2010), Development of a cloud-top height estimation method by geostationary satellite split-window measurements trained with Cloudsat data, *J. Appl. Meteorol. Clim.*, 49(9), 2035–2049, doi:10.1175/2010JAMC2287.1.
- Haywood, J. M., et al. (2010), Observations of the eruption of the Sarychev volcano and simulations using the HadGEM2 climate model, *J. Geophys. Res.*, 115, D21212, doi:10.1029/2010JD014447.
- Heard, I. P. C., A. J. Manning, J. M. Haywood, C. Witham, A. Redington, A. Jones, L. Clarisse, and A. Bourassa (2012), A comparison of atmospheric dispersion model predictions with observations of SO<sub>2</sub> and sulphate aerosol from volcanic eruptions, *J. Geophys. Res.*, 117, D00U22, doi:10.1029/2011JD016791.
- Hilton, F., et al. (2012), Hyperspectral earth observation from IASI: Five years of accomplishments, *Bull. Am. Meteorol. Soc.*, 93(3), 347–370, doi:10.1175/BAMS-D-11-00027.1.

- Holton, J. R., P. H. Haynes, M. E. McIntyre, A. R. Douglass, R. B. Rood, and L. Pfister (1995), Stratosphere-troposphere exchange, *Rev. Geophys.*, 33(4), 403–439, doi:10.1029/95RG02097.
- Jégou, F., et al. (2013), Stratospheric aerosols from the Sarychev volcano eruption in the 2009 Arctic summer, *Atmos. Chem. Phys.*, 13(13), 6533–6552, doi:10.5194/acp-13-6533-2013.
- Kalnay, E., et al. (1996), The NCEP/NCAR 40-year reanalysis project, *Bull. Am. Meteorol. Soc.*, 77(3), 437–471, doi:10.1175/1520-0477(1996)077<0437:TNYRP>2.0.CO;2.
- Karagulian, F., L. Clarisse, C. Clerbaux, A. J. Prata, D. Hurtmans, and P.-F. Coheur (2010), Detection of volcanic SO<sub>2</sub>, ash, and H<sub>2</sub>SO<sub>4</sub> using the Infrared Atmospheric Sounding Interferometer (IASI), *J. Geophys. Res.*, 115, D00L02, doi:10.1029/2009JD012786.
- Kravitz, B., A. Robock, and A. Bourassa (2010), Negligible climatic effects from the 2008 Okmok and Kasatochi volcanic eruptions, *J. Geophys. Res.*, 115, D00L05, doi:10.1029/2009JD013525.
- Kravitz, B., et al. (2011), Simulation and observations of stratospheric aerosols from the 2009 Sarychev volcanic eruption, *J. Geophys. Res.*, 116, D18211, doi:10.1029/2010JD015501.
- Livesey, N. J., et al. (2011), Earth Observing System (EOS) Aura Microwave Limb Sounder (MLS) version 3.3 level 2 data quality and description document, *JPL D-33509*, Jet Propul. Lab., Calif. Inst. of Technol., Pasadena.
- Mateshvili, N., et al. (2013), Nabro volcano aerosol in the stratosphere over Georgia, South Caucasus from ground-based spectrometry of twilight sky brightness, *Atmos. Meas. Tech.*, 6(3), 2563–2576, doi:10.5194/amt-6-2563-2013.
- McCormick, M. P., and R. E. Veiga (1992), SAGE II measurements of early Pinatubo aerosols, *Geophys. Res. Lett.*, 19(2), 155–158, doi:10.1029/91GL02790.
- O'Neill, N. T., et al. (2012), Properties of Sarychev sulphate aerosols over the Arctic, *J. Geophys. Res.*, 117, D04203, doi:10.1029/2011JD016838.
- Oppenheimer, C. (1998), Volcanological applications of meteorological satellites, *Int. J. Remote Sens.*, 19(15), 2829–2964, doi:10.1080/014311698214307.
- Palm, S. P., M. D. Fromm, and J. Spinhirne (2005), Observations of antarctic polar stratospheric clouds by the Geoscience Laser Altimeter System (GLAS), *Geophys. Res. Lett.*, 32, L22S04, doi:10.1029/2005GL023524.
- Poole, L. R., and M. C. Pitts (1994), Polar stratospheric cloud climatology based on stratospheric aerosol measurement II observations from 1978 to 1989, *J. Geophys. Res.*, 99(D6), 13,083–13,089, doi:10.1029/94JD00411.
- Rybin, A., M. Chibisova, P. Wbley, T. Steensen, P. Izbekov, C. Neal, and V. Realmuto (2011), Satellite and ground observations of the June 2009 eruption of Sarychev Peak volcano, Matua Island, Central Kuriles, *Bull. Volcanol.*, 73(9), 1377–1392, doi:10.1007/s00445-011-0481-0.
- Sassen, K., M. K. Griffin, and G. C. Dodd (1990), Optical scattering and microphysical properties of subvisual cirrus clouds, and climatic implications, *J. Appl. Meteorol.*, 28, 91–98, doi:10.1175/1520-0450(1989)028<0091:OSAMPO>2.0.CO;2.
- Sawamura, P., et al. (2012), Stratospheric AOD after the 2011 eruption of Nabro volcano measured by lidars over the Northern Hemisphere, *Environ. Res. Lett.*, 7(3), 034,013, doi:10.1088/1748-9326/7/3/034013.
- Schmetz, J., P. Pili, S. Tjemkes, D. Just, J. Kerkmann, S. Rota, and A. Rateri (2002), Supplement to an introduction to Meteosat Second Generation (MSG) radiometric performance of SEVIRI, *Bull. Am. Meteorol. Soc.*, 83(7), 991, doi:10.1175/BAMS-83-7-Schmetz-1.
- Sherwood, S. C., J.-H. Chae, P. Minnis, and M. McGill (2004), Underestimation of deep convective cloud tops by thermal imagery, *Geophys. Res. Lett.*, 31, L11102, doi:10.1029/2004GL019699.
- Siddaway, J. M., and S. V. Petelina (2011), Transport and evolution of the 2009 Australian Black Saturday bushfire smoke in the lower stratosphere observed by OSIRIS on Odin, *J. Geophys. Res.*, 116, D06203, doi:10.1029/2010JD015162.
- SIGVP (2011), *Smithsonian Institution Global Volcanism Program*. [Available at <http://www.volcano.si.edu/world/volcano.cfm?vnum=0201-101>; volpage=weekly.]
- Thomason, L., and T. Peter (Eds.) (2006), Assessment of stratospheric aerosol properties (ASAP), *SPARC Rep. 4, WMO/TD 1295, Tech Rep. WCRP-124*, Geneva, Switzerland.
- Treffiesen, R. E., L. W. Thomason, J. Ström, A. B. Herber, S. P. Burton, and T. Yamanouchi (2006), Stratospheric aerosol and gas experiment (SAGE) II and III aerosol extinction measurements in the Arctic middle and upper troposphere, *J. Geophys. Res.*, 111, D17203, doi:10.1029/2005JD006271.
- Tupper, A., and R. Wunderman (2009), Reducing discrepancies in ground and satellite-observed eruption heights, *J. Volcanol. Geotherm. Res.*, 186(1), 22–31, doi:10.1016/j.jvolgeores.2009.02.015.
- Uchino, O., et al. (2012), On recent (2008–2012) stratospheric aerosols observed by lidar over Japan, *Atmos. Chem. Phys.*, 12(24), 11,975–11,984, doi:10.5194/acp-12-11975-2012.
- Vernier, J. P., L. W. Thomason, T. D. Fairlie, P. Minnis, R. Palikonda, and K. M. Bedka (2013), Comment on “Large volcanic aerosol load in the stratosphere linked to Asian monsoon transport”, *Science*, 339(6120), 647, doi:10.1126/science.1227817.
- Wang, P.-H., M. P. McCormick, P. Minnis, G. S. Kent, G. K. Yue, and K. M. Skeens (1995), A method for estimating vertical distribution of the SAGE II opaque cloud frequency, *Geophys. Res. Lett.*, 22(3), 243–246, doi:10.1029/94GL02992.
- Wang, P.-H., R. E. Veiga, L. B. Vann, P. Minnis, and G. S. Kent (2001), A further study of the method for estimation of SAGE II opaque cloud occurrence, *J. Geophys. Res.*, 106(D12), 12,603–12,613, doi:10.1029/2001JD900138.
- Waters, J. W., et al. (2006), The Earth observing system microwave limb sounder (EOS MLS) on the Aura satellite, *IEEE Trans. Geosci. Remote Sens.*, 44(5), 1075–1092, doi:10.1109/TGRS.2006.873771.
- Welton, E. J., J. R. Campbell, J. D. Spinhirne, and V. S. Scott III (2001), Global monitoring of clouds and aerosols using a network of micropulse lidar systems, in *Second International Asia-Pacific Symposium on Remote Sensing of the Atmosphere, Environment, and Space*, edited by U. N. Singh, T. Itabe, and N. Sugimoto, pp. 151–158, Int. Soc. for Optics and Photonics, Bellingham, Wash.
- Winker, D. M., M. A. Vaughan, A. Omar, Y. Hu, K. A. Powell, Z. Liu, W. H. Hunt, and S. A. Young (2009), Overview of the CALIPSO mission and CALIOP data processing algorithms, *J. Atmos. Ocean. Tech.*, 26(11), 2310–2323, doi:10.1175/2009JTECHA1281.1.